Chapter 6

Flow Structure

Simulations of axial flow over cylinders performed using the method described in chapter 2 produce a temporal sequence of three-dimensional vorticity, velocity and, if required, pressure fields. The computed flow fields capture all of the significant spatial scales of turbulence throughout the full computational domain. The data may be analysed in a variety of ways to reveal features of the instantaneous flow that are obscured by aggregate statistics such as those discussed in the preceding chapters.

The initial section of the current chapter presents slices of instantaneous flow fields from two axial-flow simulations with similar Reynolds numbers (δ^+) and different curvature parameters (a^+, δ/a). Comparison of the two flows reveals the qualitative effects of transverse boundary layer curvature on instantaneous flow structures. The second section considers statistical analysis of the typical sizes of flow structures, by examination of the streamwise and spanwise correlation functions for a range of cylinder and plane-channel simulations. The third section examines the spatial structure of conditionally averaged turbulent burst events. The main findings are summarised at the end of the chapter.

6.1 Instantaneous Flow Fields

In this section, instantaneous flow fields are compared between two of the present axial-flow simulations that have been advanced to the statistically-steady state. Both flows have similar values of δ^+, widely different values of a^+, and δ/a much larger than unity. Neves [1992] undertakes a similar exercise, but between flows with smaller δ^+ and a narrower a^+ interval. The two simulations considered here are $Re_a = 311$, $b/a = 41$ and $Re_a = 2600$, $b/a = 6$. The mean-flow parameters given by table 4.1 for the former case are $a^+ = 21.0$, $\delta/a = 27.6$, $\delta^+ = 580$ and for the latter case are $a^+ = 131$, $\delta/a = 4.0$, $\delta^+ = 527$.

Visualisation of the flows is achieved by means of contour lines and coloured shading on slices of the instantaneous flow fields. Flow variables are presented in non-dimensional form with respect to wall variables. The contour and colour levels are the same for all views of a given variable (velocity, vorticity or pressure) in both flows. The in-plane motion of structures in the velocity field is represented by small arrows, whose sizes and directions are proportional to the local velocity vector. All figures are drawn to the same spatial scale based on wall-units; the cylinder size is therefore proportional to a^+.

Figures 6.1 and 6.2 show axial velocity fluctuations on a transverse (r-θ) slice through each of the two flows. The axial location ($z^+ = 1250$) is reported so that comparison can be made with the streamwise slices shown in later figures. Evident in both of the present figures are bursts of low-speed fluid at various stages of ejection from the inner layer, as are regions of high-speed fluid sweeping inwards from the outer layer. The velocity structures are small and finely spaced near the cylinder wall, while further out, the structures are typically larger. For small a^+ (figure 6.2), the flow is nearly quiescent in the outer portion of the layer. The number of distinct structures and corresponding complexity of the flow appears to increase with a^+. The largest structures have similar sizes in both flows, but in the case of small a^+, some of the structures are considerably larger than the cross-sectional area of the cylinder.

Axial velocity fluctuations on a streamwise slice along the cylinder axis (Y-z plane) are shown in figures 6.3 and 6.4 for flow with large and small a^+, respectively. Near the cylinder wall, the streak-like structures that are in contact with the wall are typically much longer in the axial (z) direction than they are tall in the wall-normal (Y) direction. Structures that lift away from the wall gradually lose their streak-like shape as they interact with other structures or diffuse under the action of viscosity. The largest structures in both flows have similar sizes, but in the case

of small a^+ (figure 6.4), the length of the structures is many times greater than the cylinder radius. There appear to be fewer distinct regions of low- and high-speed fluid when a^+ is small. The difference in the number of structures is reflected in the skewness and flatness profiles of the velocity fluctuations, as discussed earlier in section 4.5.

It is interesting to note that in the flow shown in figure 6.4, there is a strong tendency for low-speed fluid on one side of the cylinder to be associated with high-speed fluid on the opposite side. This observation suggests the occurrence of large-scale cross-flows at irregular intervals along the cylinder axis. In support of this notion, the velocity vectors on the transverse slice in figure 6.2 indicate the presence of a large-scale cross-flow which is superimposed onto the motion of the smaller scales. The effects of cross-flow are much less obvious in figures 6.1 and 6.3. It seems that cross-flow is significant mainly when a^+ is small and δ/a is large.

Figure 6.5 shows axial velocity fluctuations on unwrapped cylindrical surfaces at $y^+ = 15$ in both flows. The typical size and shape of the low- and high-speed streaks is similar for large and small a^+. In the case of $a^+ = 21$ (figure 6.5b), there are approximately two low-speed and two high-speed streaks distributed around the cylinder. For $a^+ = 131$ (figure 6.5a), the circumferential width of the slice in wall units is approximately quadrupled, and so is the number of streaks.

The radial component of instantaneous velocity is shown in figures 6.6–6.10 for the same slice planes as those used to present the axial velocity. Near the outer boundary of the computational domain, the radial motion of structures appears not to be inhibited by the presence of the boundary; this behaviour is an intentional characteristic of the simulation procedure. Relative to flow with large a^+ (figures 6.6, 6.8 and 6.10a), the radial velocity fluctuations are weaker and more sporadic when a^+ is small (figures 6.7, 6.9 and 6.10b). In this regard, the instantaneous flow structures are consistent with the RMS velocity and flatness profiles presented in sections 4.3 and 4.5. In figures 6.7 and 6.9, where $a^+ = 21$, the regions of oppositely directed radial velocity on opposite sides of the cylinder constitute further evidence for the occurrence of large-scale cross-flows in flows with small a^+ and large δ/a. Another noteworthy observation relates to the near-wall slices shown in figure 6.10, where streaks of intense radial velocity often occur in bi-directional pairs. These pairs suggest the presence of streamwise vorticity.

Azimuthal velocity fluctuations are shown in figures 6.11 and 6.12 on the same transverse slice as before. Coherent regions of azimuthal velocity are strongly curved around the cylinder. The curvature of the structures suggests that the mean velocity gradient provides resistance to motion of fluid in the radial direction.

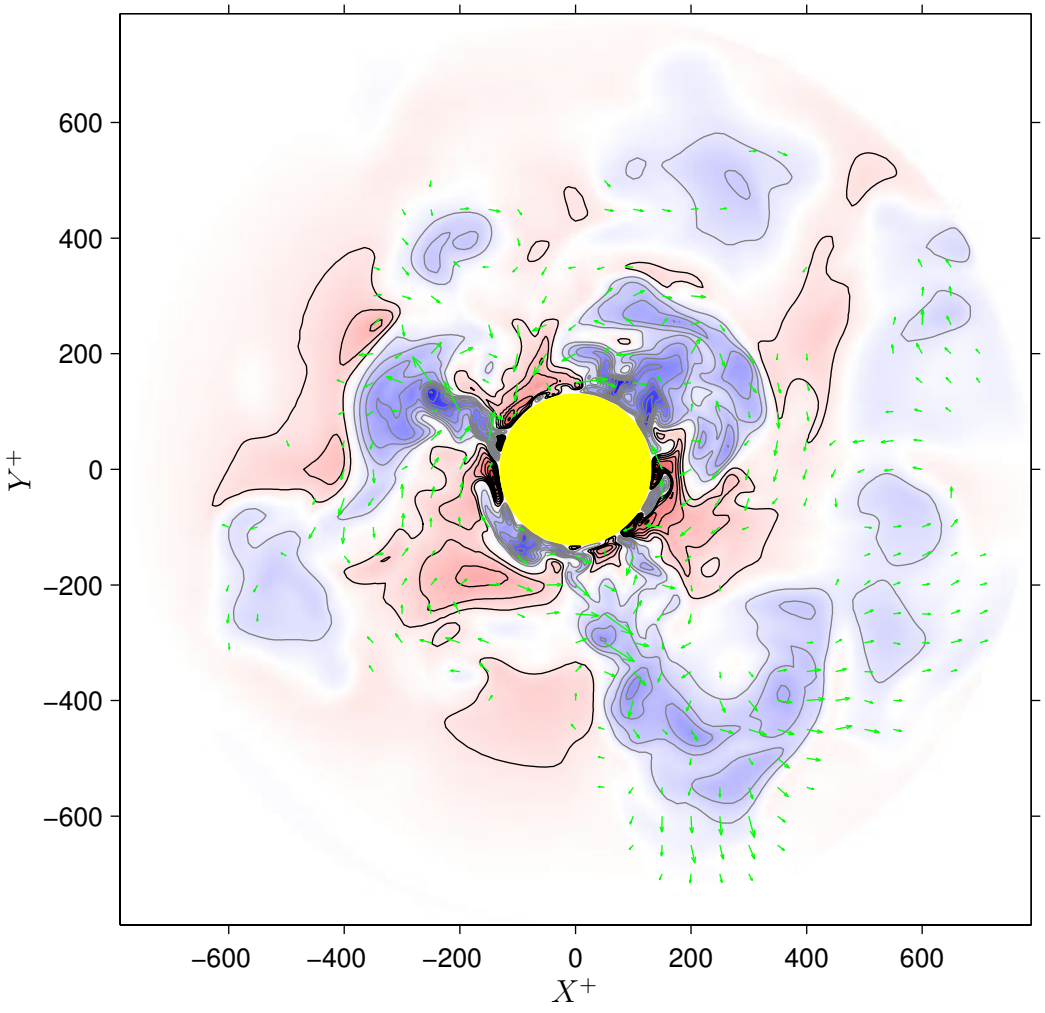

Figure 6.1: Instantaneous axial velocity fluctuations in plane $z^+ = 1250$ for $Re_a = 2600$, $b/a = 6$. Green arrows depict relative magnitude and direction of in-plane velocity. The contour increment is $0.6u_\tau$. Black contours and red shading indicate $u_z > 0$, grey contours and blue shading indicate $u_z < 0$.

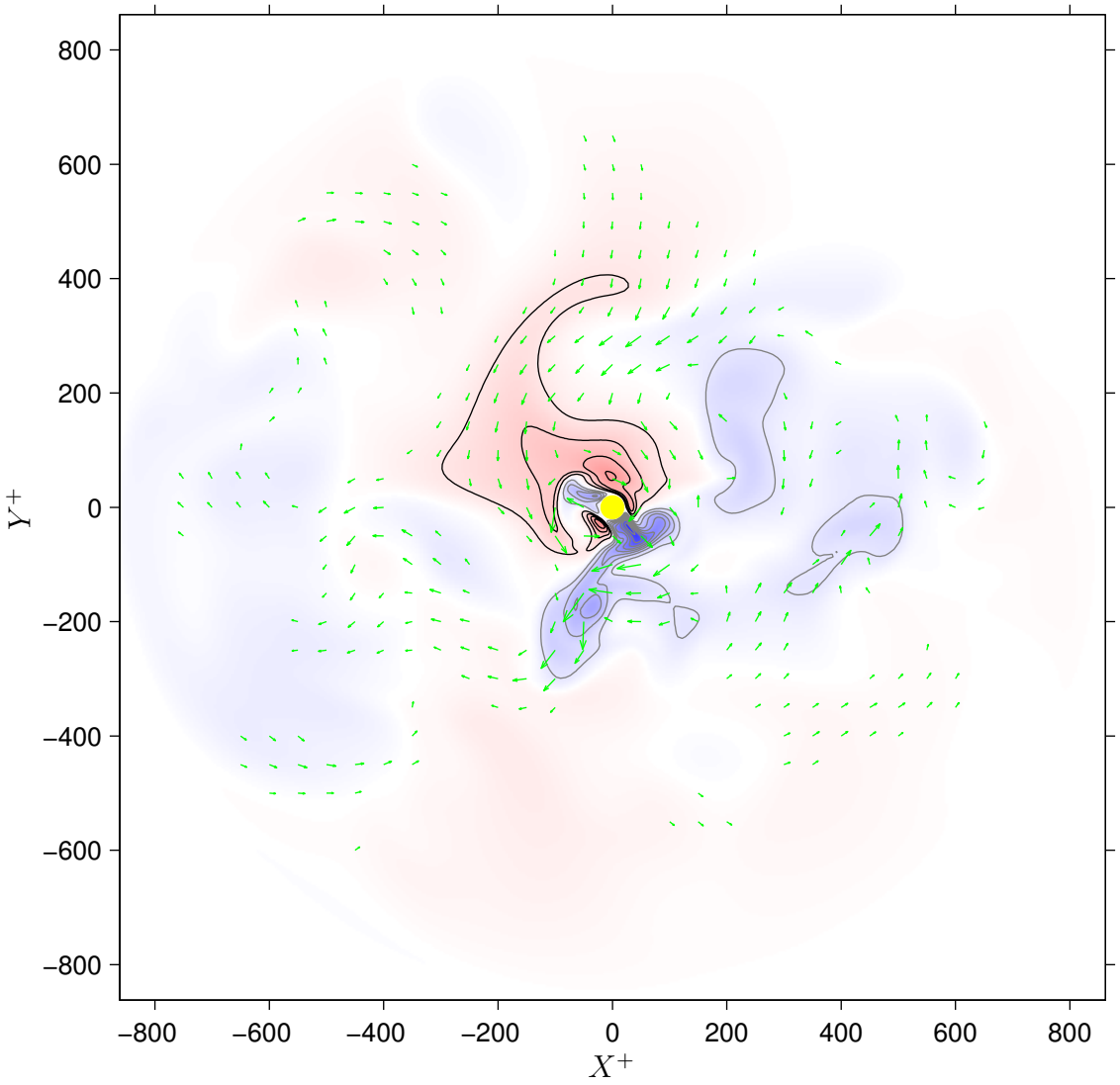

Figure 6.2: Instantaneous axial velocity fluctuations in plane $z^+ = 1250$ for $Re_a = 311$, $b/a = 41$. Green arrows depict relative magnitude and direction of in-plane velocity. The contour increment is $0.6u_\tau$. Black contours and red shading indicate $u_z > 0$, grey contours and blue shading indicate $u_z < 0$.

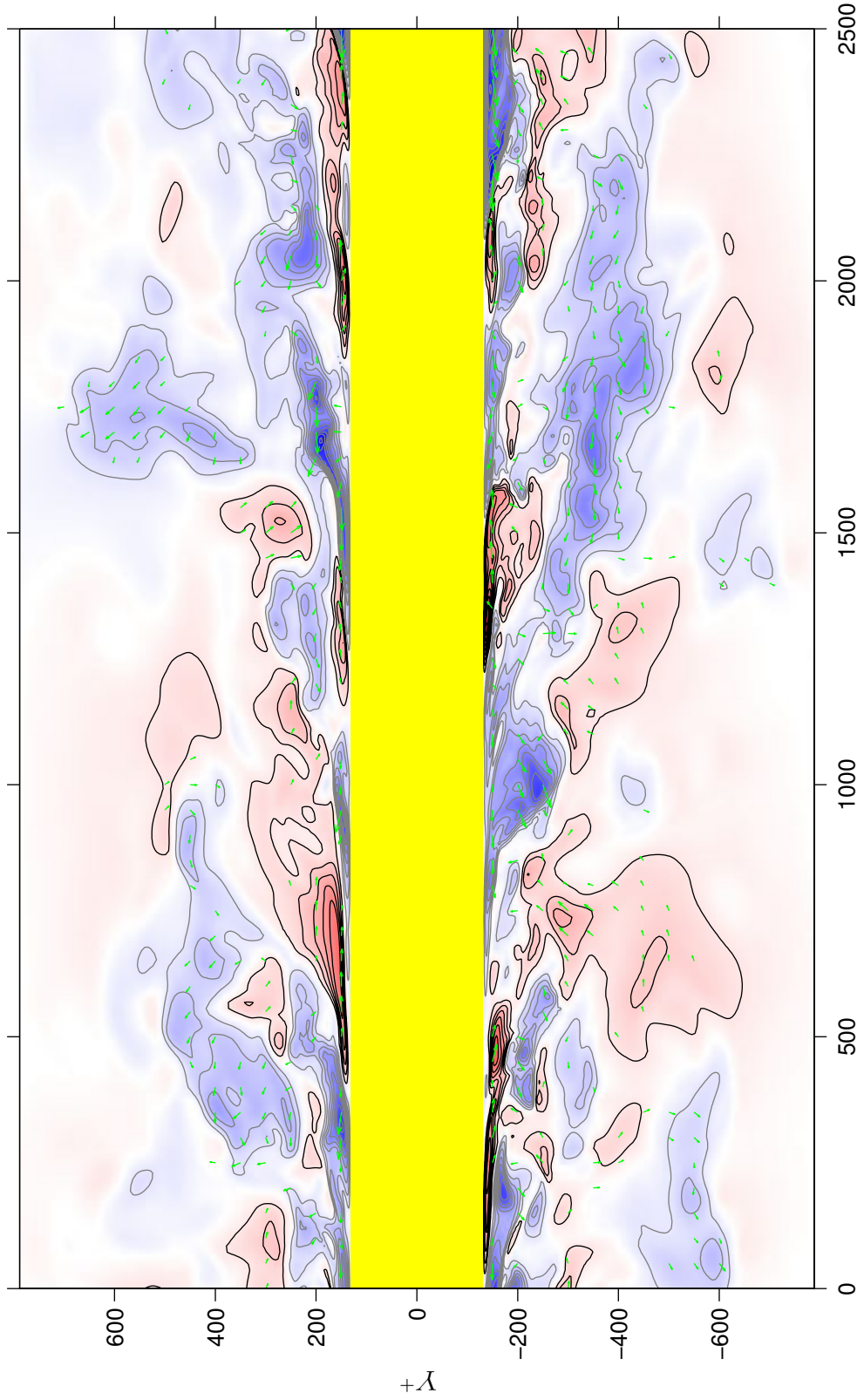

Figure 6.3: Instantaneous axial velocity fluctuations in plane $X = 0$ for $Re_a = 2600$, $b/a = 6$. Legend as for figure 6.1.

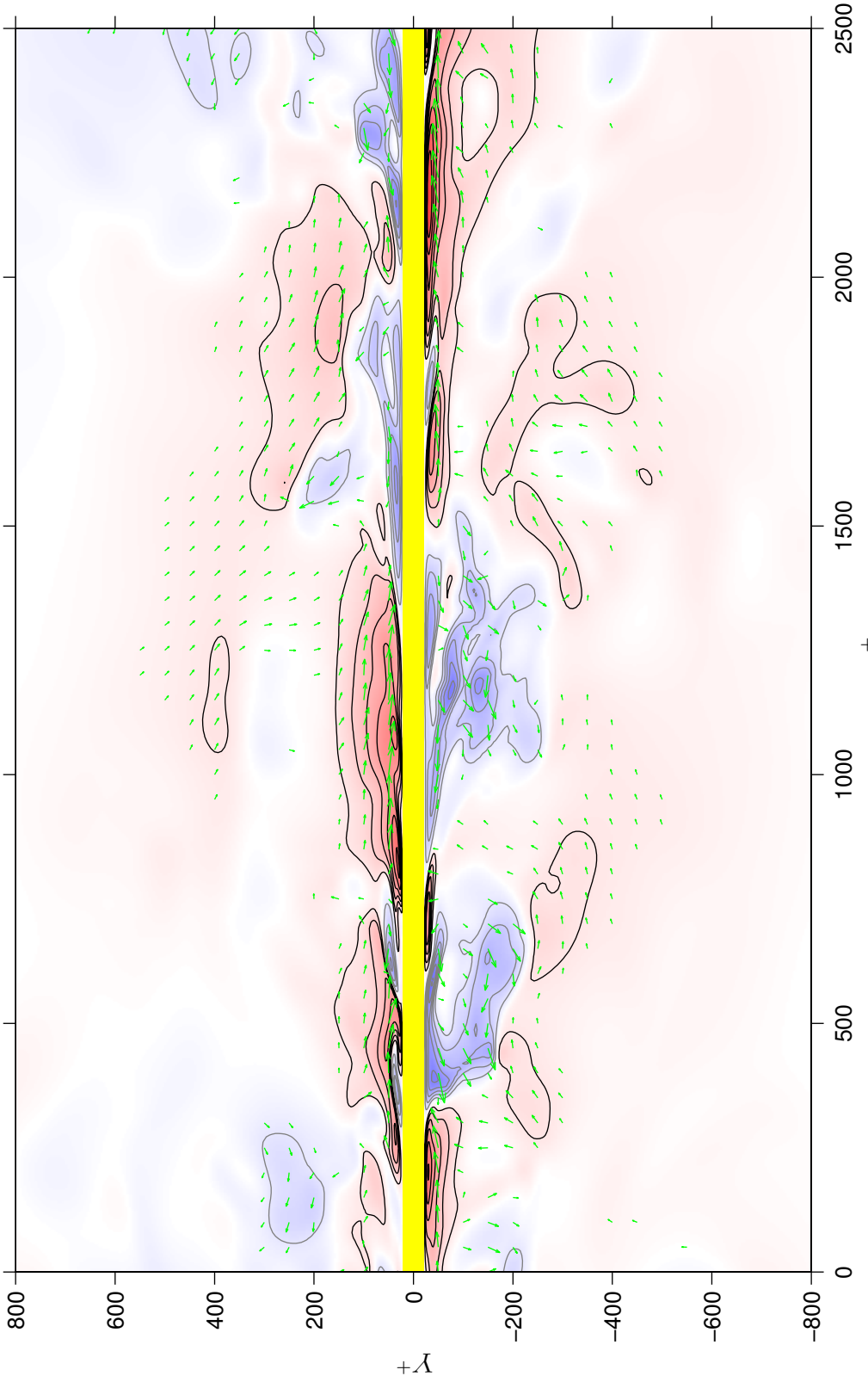

Figure 6.4: Instantaneous axial velocity fluctuations in plane $X = 0$ for $Re_a = 311$, $b/a = 41$. Legend as for figure 6.2.

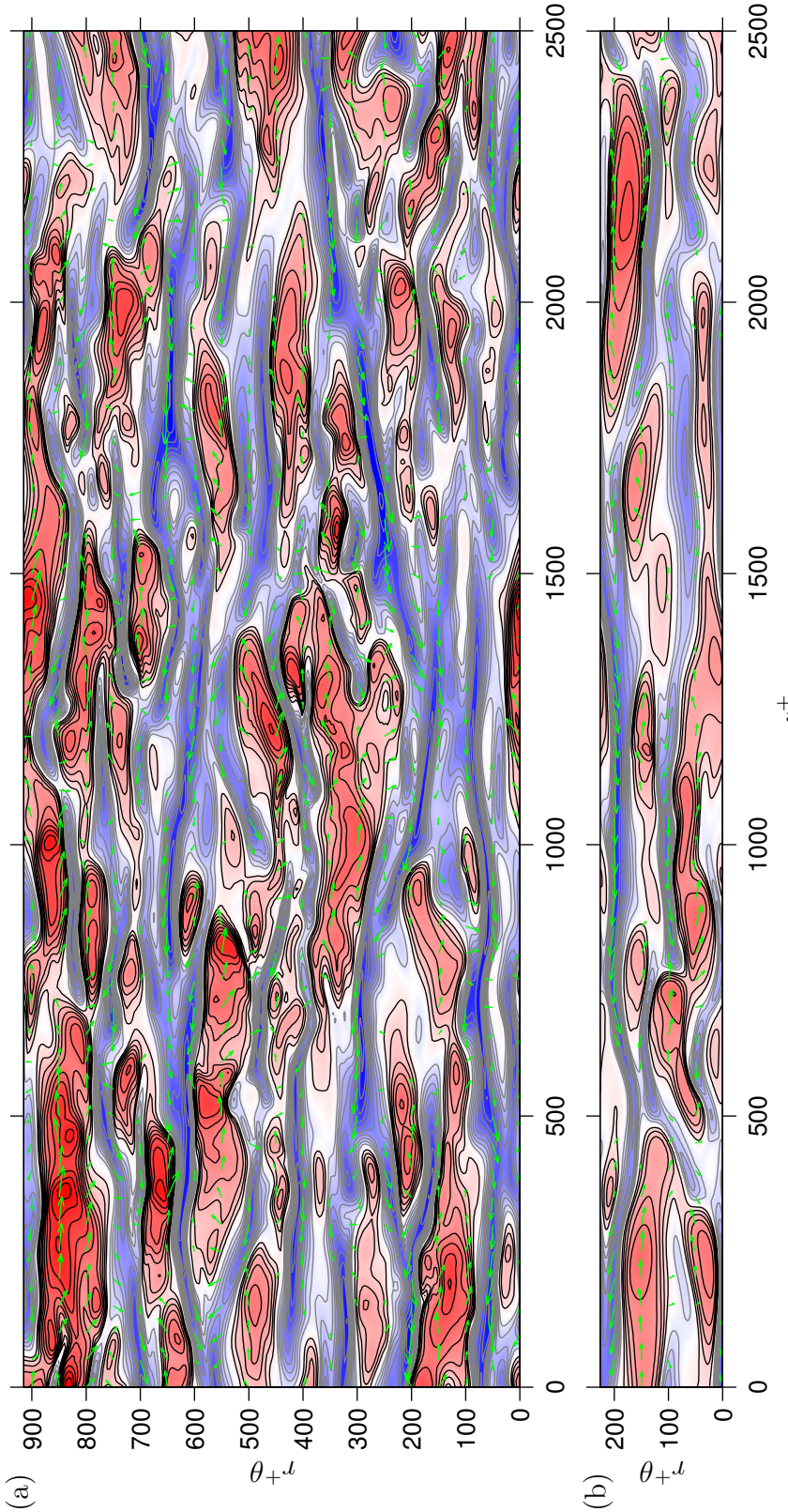

Figure 6.5: Instantaneous axial velocity fluctuations at $y^+ = 15$ for (a) $Re_a = 2600$, $b/a = 6$ and (b) $Re_a = 311$, $b/a = 41$. Green arrows depict relative magnitude and direction of in-plane velocity. The contour increment is $0.6u_\tau$. Black contours and red shading indicate $u_z > 0$, grey contours and blue shading indicate $u_z < 0$.

In figures 6.13 and 6.14, on the streamwise slice considered previously, the azimuthal velocity structures are generally aligned with one another and inclined relative to the wall. Near the wall, the inclination angle is small, while further away the angle is typically close to 45°. The interfaces between adjacent regions of positive and negative azimuthal velocity are associated with structures in the vorticity field. The alignment of vortical structures occurs as a result of vortex stretching, which acts to intensify the component of vorticity that is parallel to the axis of extension. Analyses of instantaneous vorticity fields from simulations of planar [Moin and Kim, 1985] and axisymmetric [Neves, 1992] boundary layers indicate that the vortex stretching is mainly driven by the mean shear-stress, whose principal axis is inclined at 45° to the solid wall.

Figure 6.15 shows azimuthal velocity fluctuations on the cylindrical slice at $y^+ = 15$. Compared with radial velocity fluctuations (figure 6.10), which are quite localised, the azimuthal fluctuations are coherent over large streamwise and spanwise distances. The strength and size of the azimuthal velocity structures suggests that they could play an important role in the burst-sweep cycle of turbulence generation.

The three components of vorticity are shown on a cylindrical slice, again at $y^+ = 15$, in figures 6.16–6.18. Although it is possible to find points where the axial vorticity (figure 6.16) is related to the radial velocity (figure 6.10) and other points where the radial or azimuthal vorticity (figures 6.17 and 6.18) is related to the axial velocity (figure 6.5), the connections between the vorticity and velocity slices are not as straight-forward as one might expect. The definition of vorticity involves out-of-plane velocity derivatives, which need not be related to the velocity components in the slice plane.

One noteworthy feature of the vorticity slices is the arrow-shaped structures in the azimuthal component (figure 6.18). A typical specimen is located at $z^+ = 1000$, $r^+\theta = 200$ in figure 6.18a; the head of the arrow is shaded blue and points in the direction of increasing z^+. The structures are described by Neves [1992] as being "geometrically consistent with nearly planar inclined shear layers intersected by a cylindrical surface". The present results for widely separated values of a^+ indicate that the appearance of the arrow-shaped structures does not depend on the radius of curvature $(a^+ + 15)$ of the cylindrical surface, suggesting that the structures may also occur in planar boundary layers.

The distribution of instantaneous wall-pressure in the two flows is shown in figure 6.19. The structure of the wall-pressure bears little resemblance to that of the individual velocity and vorticity component fields shown previously. The unique appearance of the wall-pressure is perhaps to be expected, because the wall-pressure

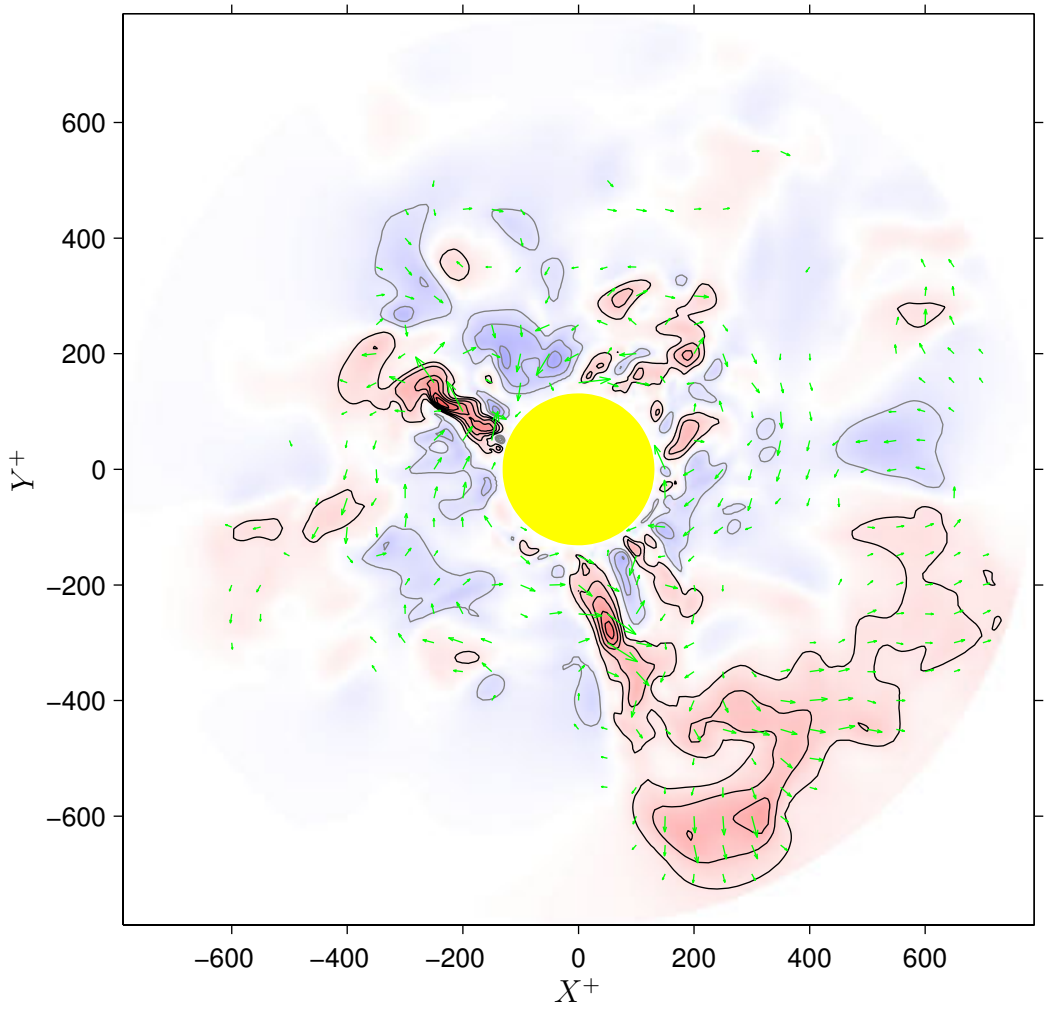

Figure 6.6: Instantaneous radial velocity in plane $z^+ = 1250$ for $Re_a = 2600$, $b/a = 6$. Green arrows depict relative magnitude and direction of in-plane velocity. The contour increment is $0.6u_\tau$. Black contours and red shading indicate $u_r > 0$, grey contours and blue shading indicate $u_r < 0$.

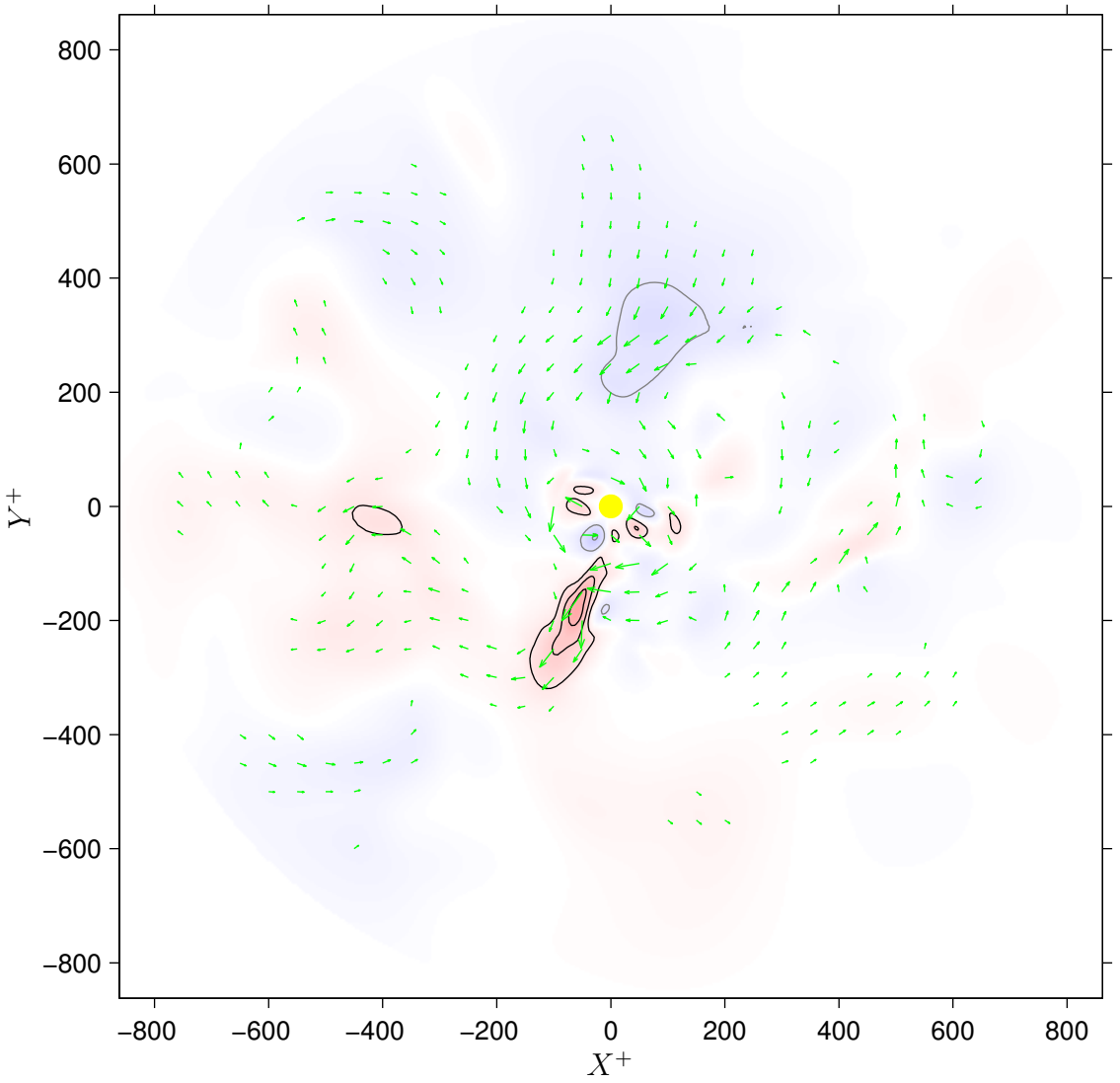

Figure 6.7: Instantaneous radial velocity in plane $z^+ = 1250$ for $Re_a = 311$, $b/a = 41$. Green arrows depict relative magnitude and direction of in-plane velocity. The contour increment is $0.6u_\tau$. Black contours and red shading indicate $u_r > 0$, grey contours and blue shading indicate $u_r < 0$.

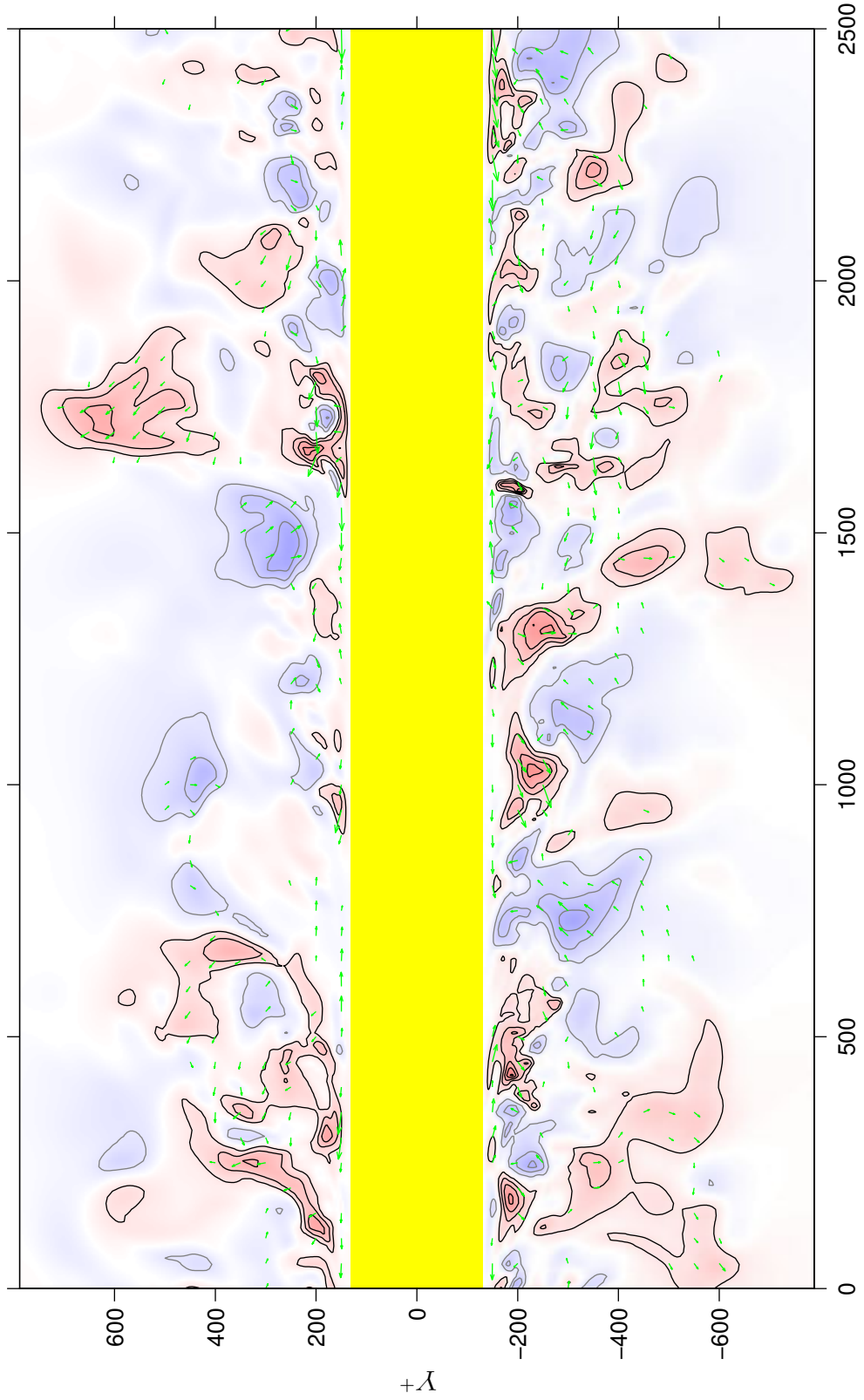

Figure 6.8: Instantaneous radial velocity in plane $X = 0$ for $Re_a = 2600$, $b/a = 6$. Legend as for figure 6.6.

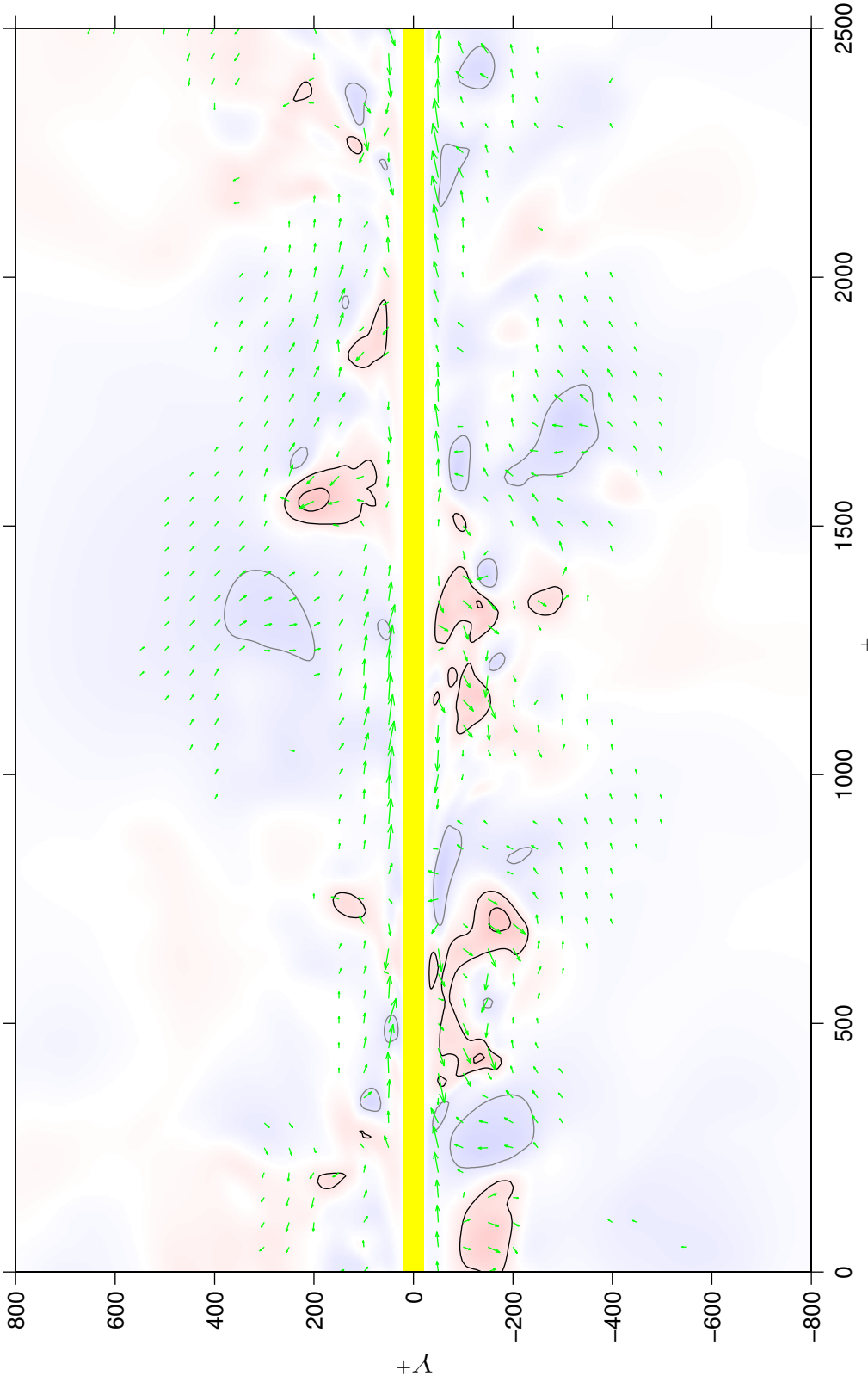

Figure 6.9: Instantaneous radial velocity in plane $X = 0$ for $Re_a = 311$, $b/a = 41$. Legend as for figure 6.7.

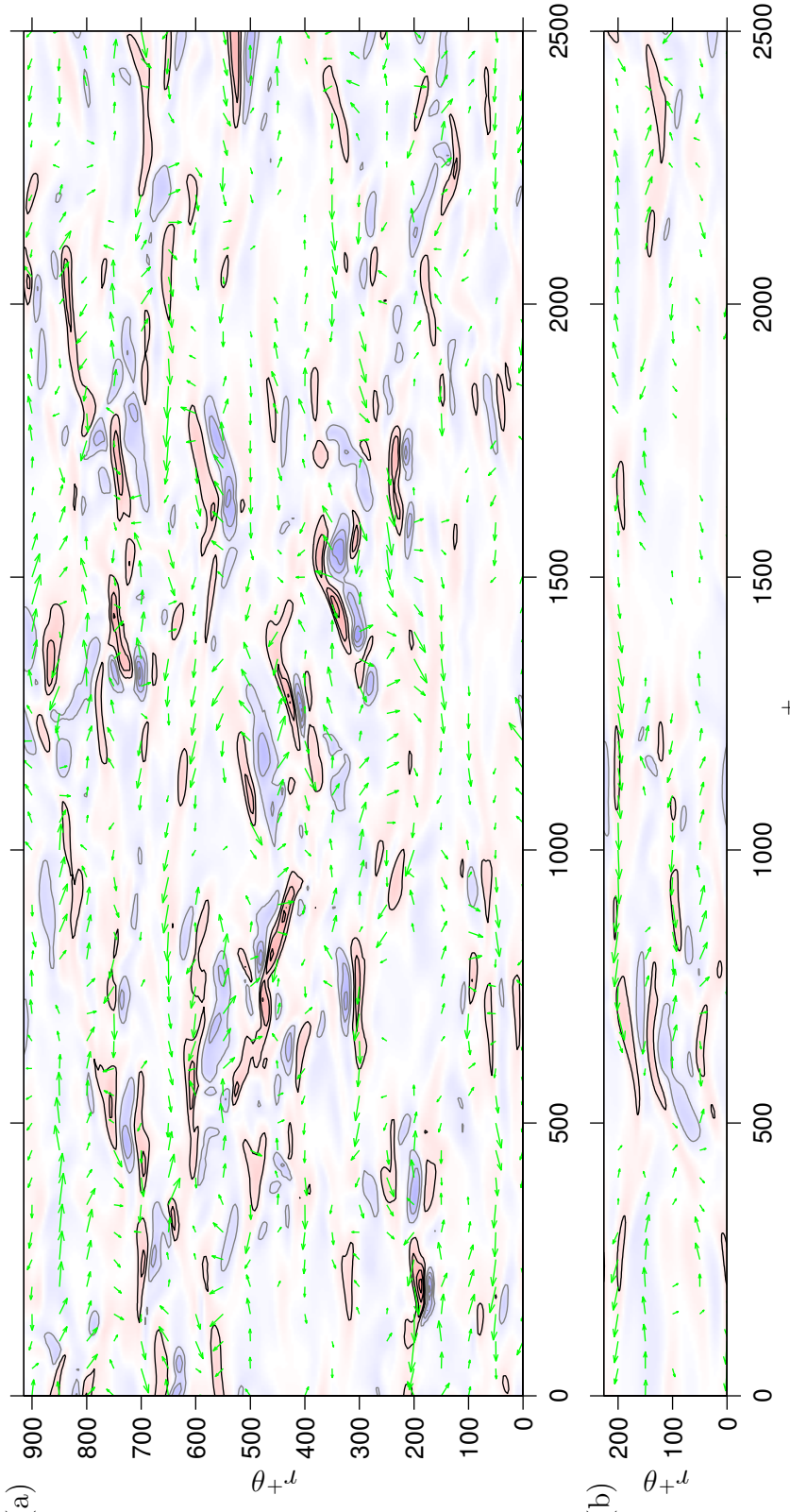

Figure 6.10: Instantaneous radial velocity at $y^+ = 15$ for (a) $Re_a = 2600$, $b/a = 6$ and (b) $Re_a = 311$, $b/a = 41$. Green arrows depict relative magnitude and direction of in-plane velocity. The contour increment is $0.6u_\tau$. Black contours and red shading indicate $u_r > 0$, grey contours and blue shading indicate $u_r < 0$.

is generated by the combined influence of spatially distributed pressure-sources, whose strength is related in a complicated fashion to local spatial derivatives of the three velocity components (see sections 5.2 and 5.3). There are significant differences between the wall-pressure distributions of the two flows. For the flow with large a^+ (figure 6.19a), coherent regions of wall-pressure are typically wider and more intense than those in the flow with small a^+ (figure 6.19b). The intensity of the structures is consistent with the RMS wall-pressure values given in figure 5.10. The width of the structures is examined further in the next section.

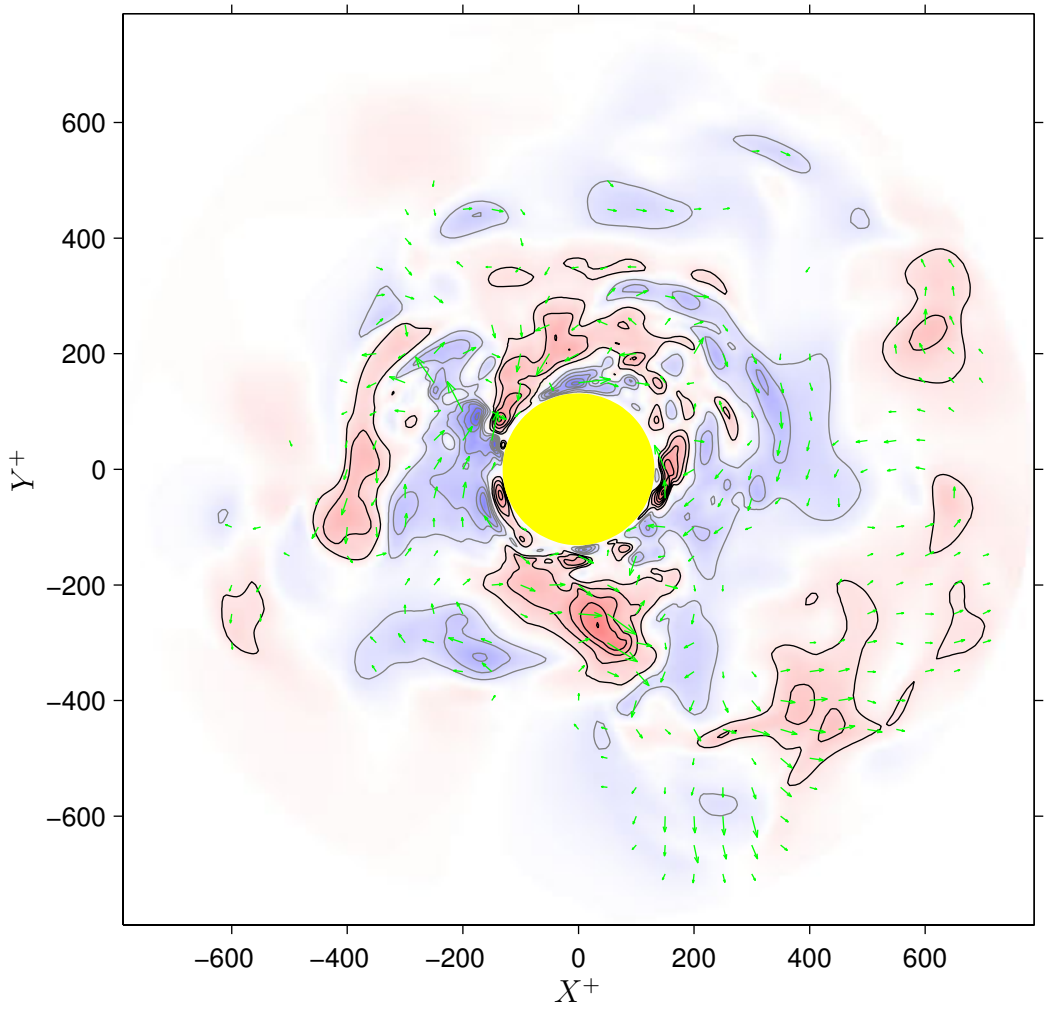

Figure 6.11: Instantaneous azimuthal velocity in plane $z^+ = 1250$ for $Re_a = 2600$, $b/a = 6$. Green arrows depict relative magnitude and direction of in-plane velocity. The contour increment is $0.6u_\tau$. Black contours and red shading indicate $u_\theta > 0$, grey contours and blue shading indicate $u_\theta < 0$.

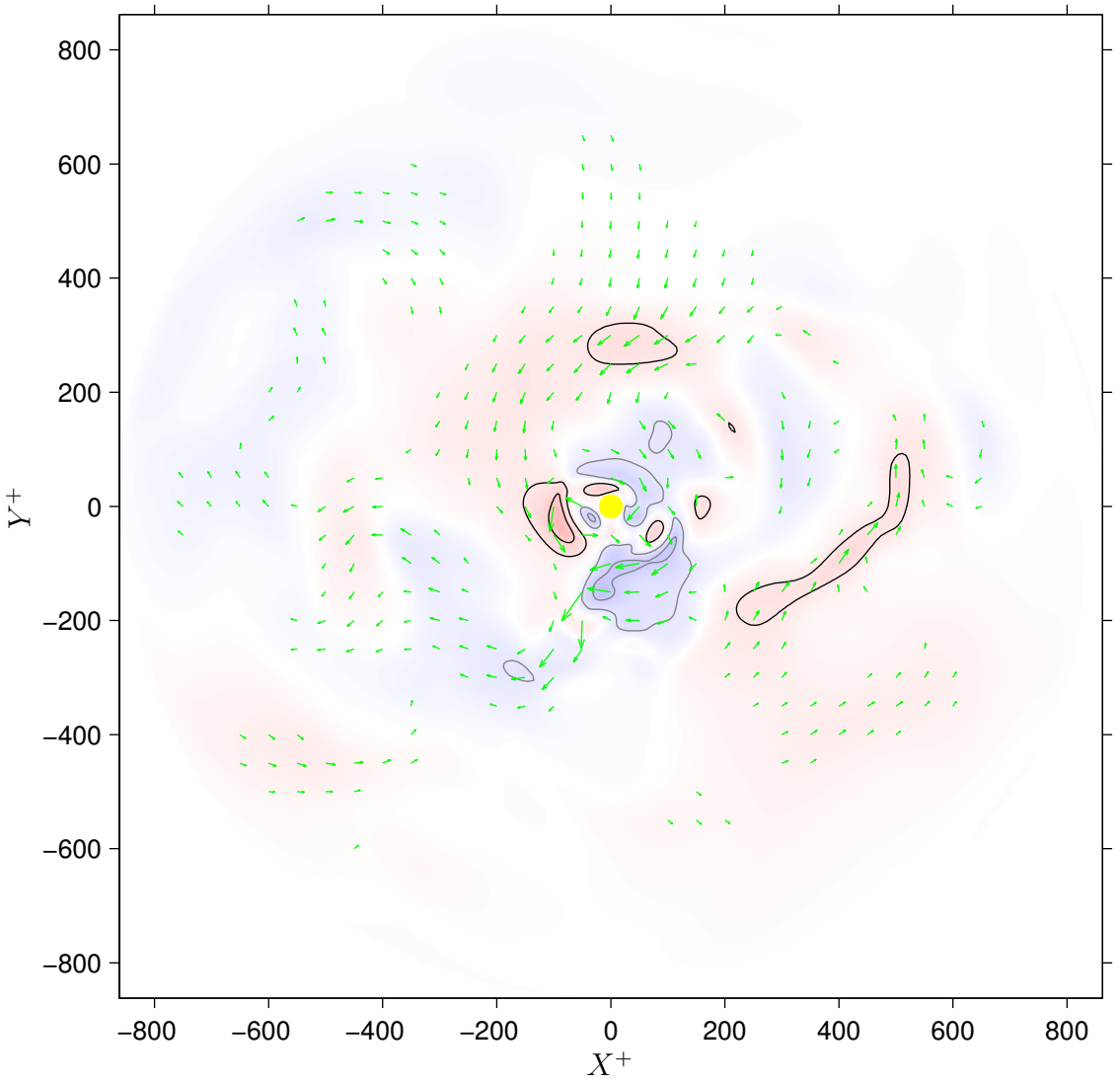

Figure 6.12: Instantaneous azimuthal velocity in plane $z^+ = 1250$ for $Re_a = 311$, $b/a = 41$. Green arrows depict relative magnitude and direction of in-plane velocity. The contour increment is $0.6u_\tau$. Black contours and red shading indicate $u_\theta > 0$, grey contours and blue shading indicate $u_\theta < 0$.

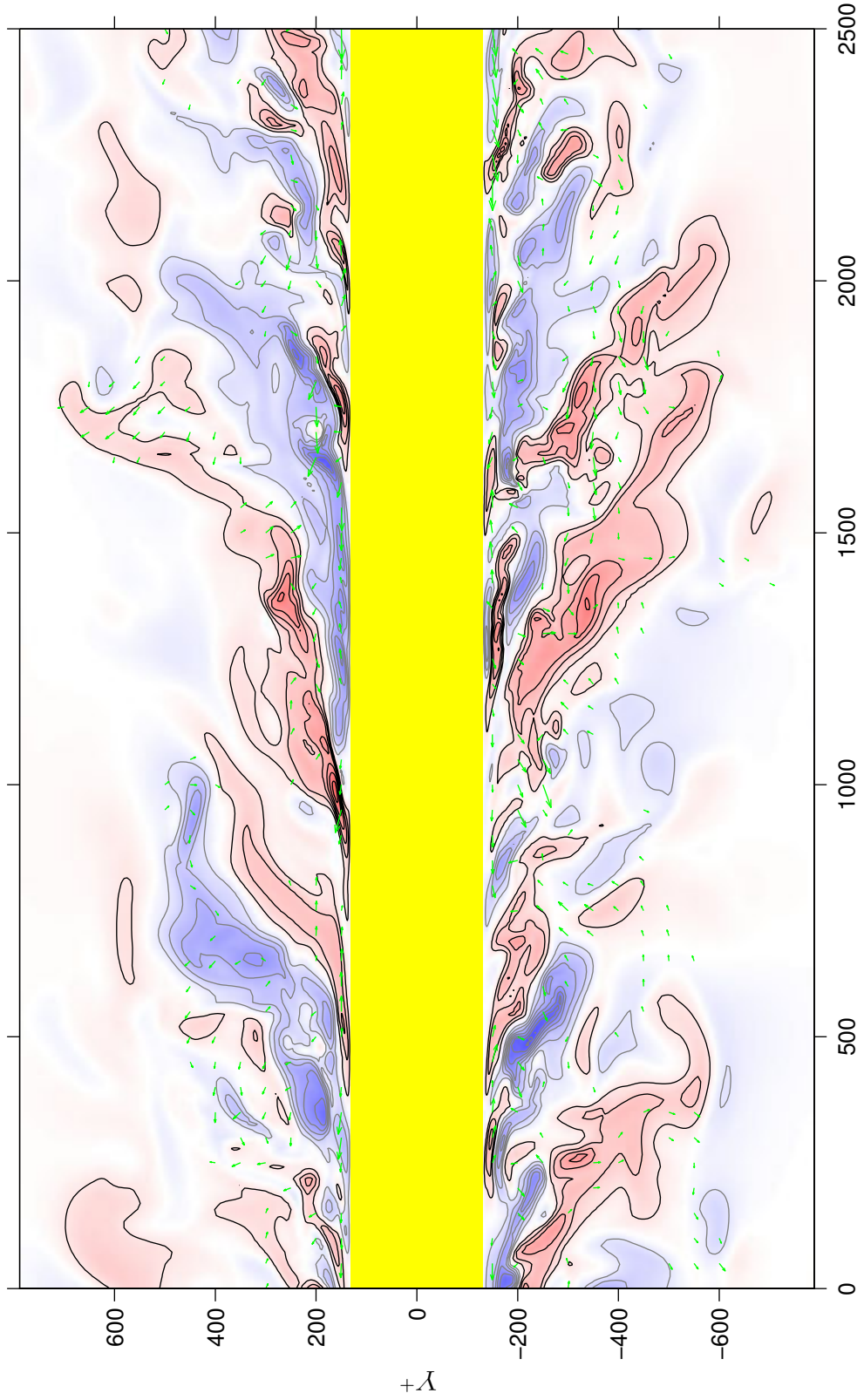

Figure 6.13: Instantaneous azimuthal velocity in plane $X = 0$ for $Re_a = 2600$, $b/a = 6$. Legend as for figure 6.11.

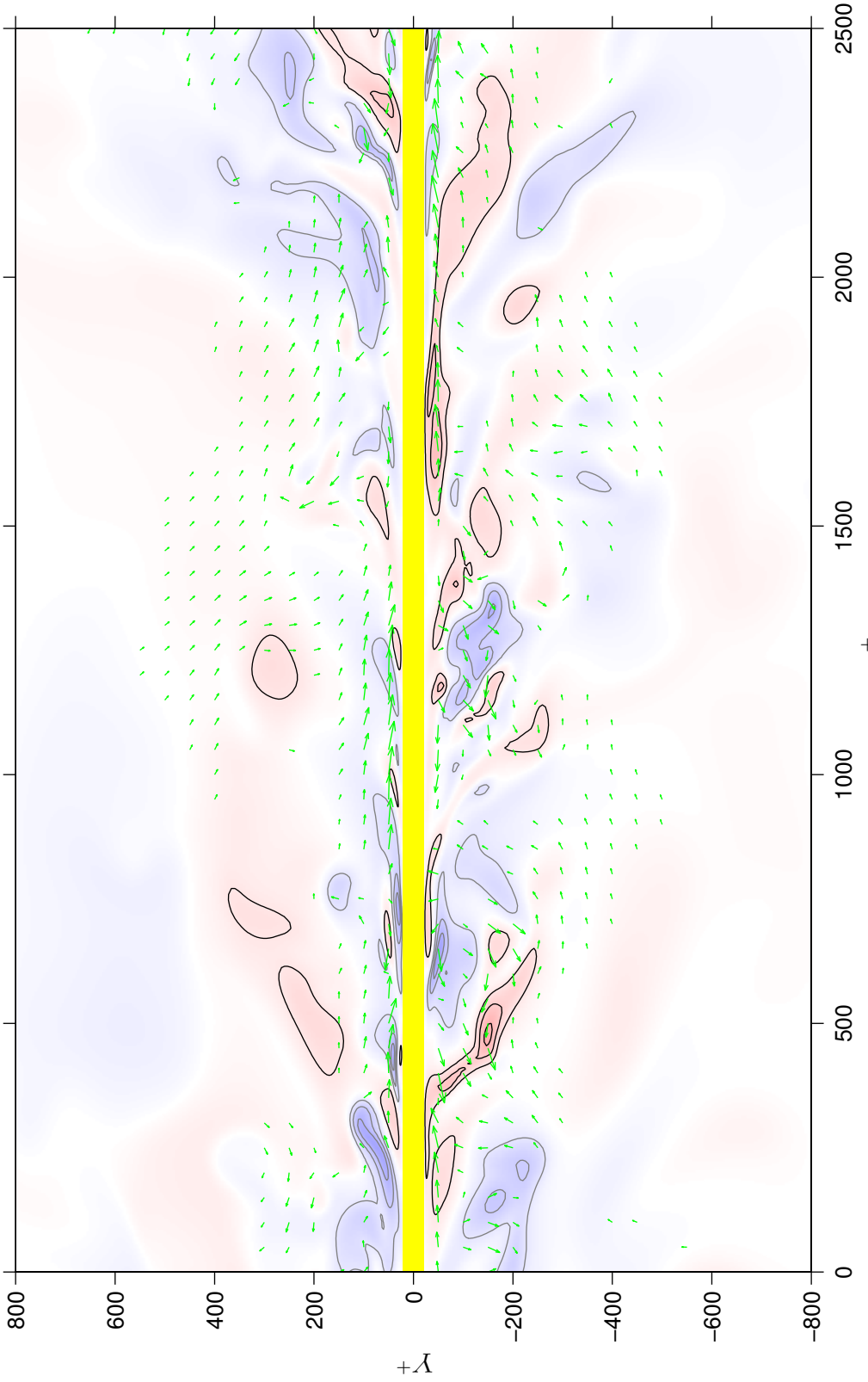

Figure 6.14: Instantaneous azimuthal velocity in plane $X = 0$ for $Re_a = 311$, $b/a = 41$. Legend as for figure 6.12.

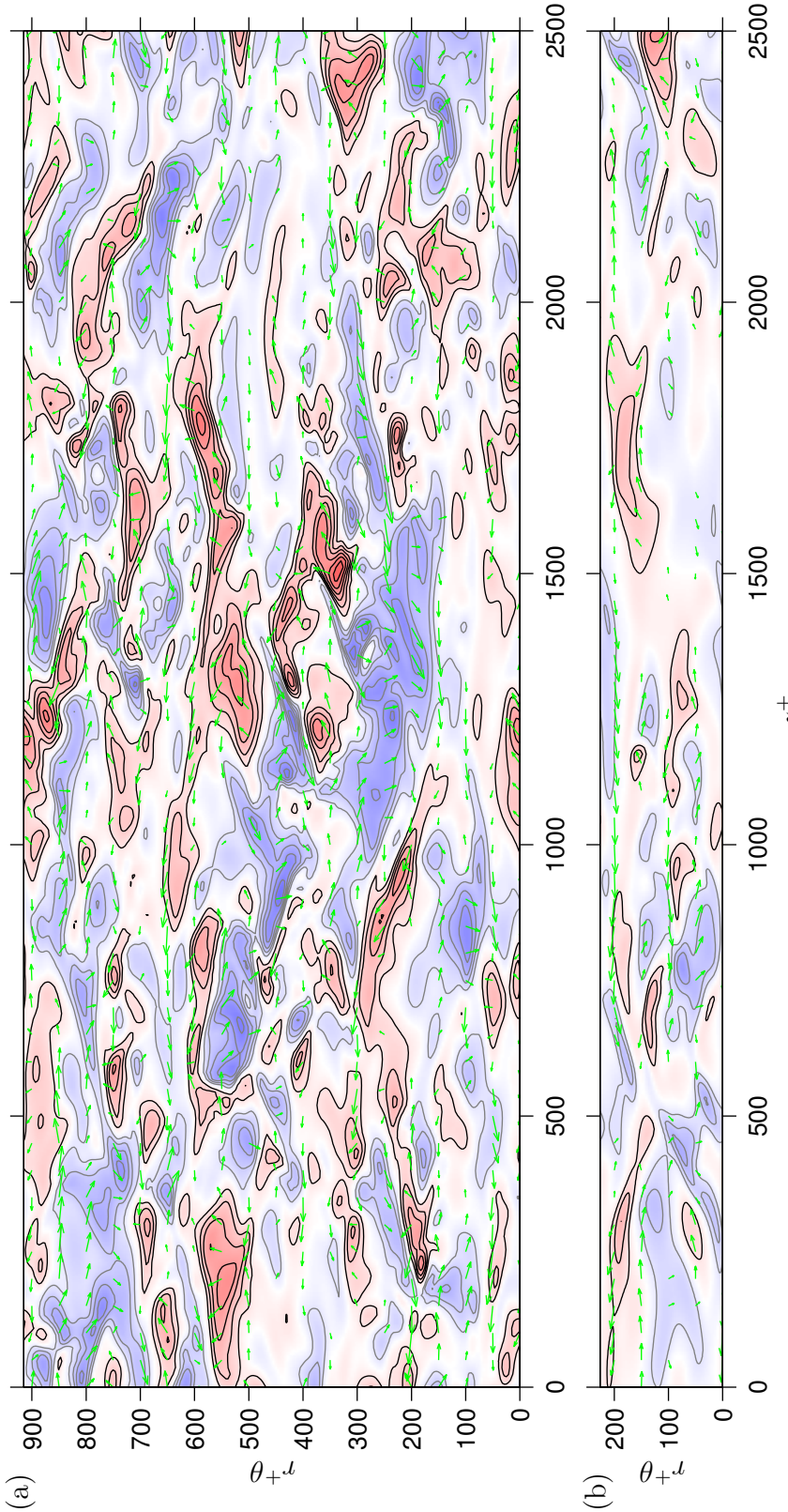

Figure 6.15: Instantaneous azimuthal velocity at $y^+ = 15$ for (a) $Re_a = 2600$, $b/a = 6$ and (b) $Re_a = 311$, $b/a = 41$. Green arrows depict relative magnitude and direction of in-plane velocity. The contour increment is $0.6u_\tau$. Black contours and red shading indicate $u_\theta > 0$, grey contours and blue shading indicate $u_\theta < 0$.

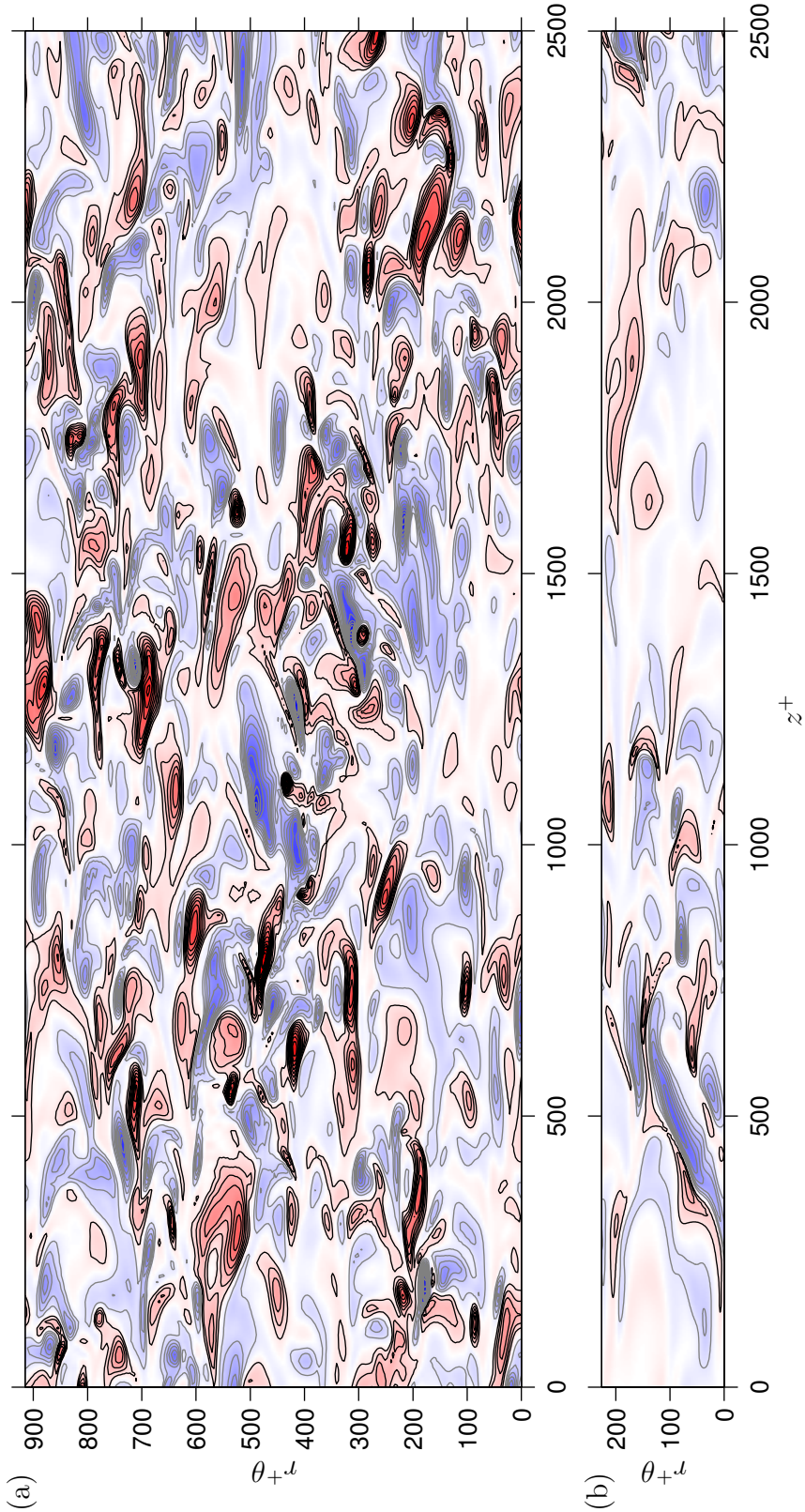

Figure 6.16: Instantaneous axial vorticity at $y^+ = 15$ for (a) $Re_a = 2600$, $b/a = 6$ and (b) $Re_a = 311$, $b/a = 41$. The contour increment is $0.06u_\tau^2/\nu$. Black contours and red shading indicate $\omega_z > 0$, grey contours and blue shading indicate $\omega_z < 0$.

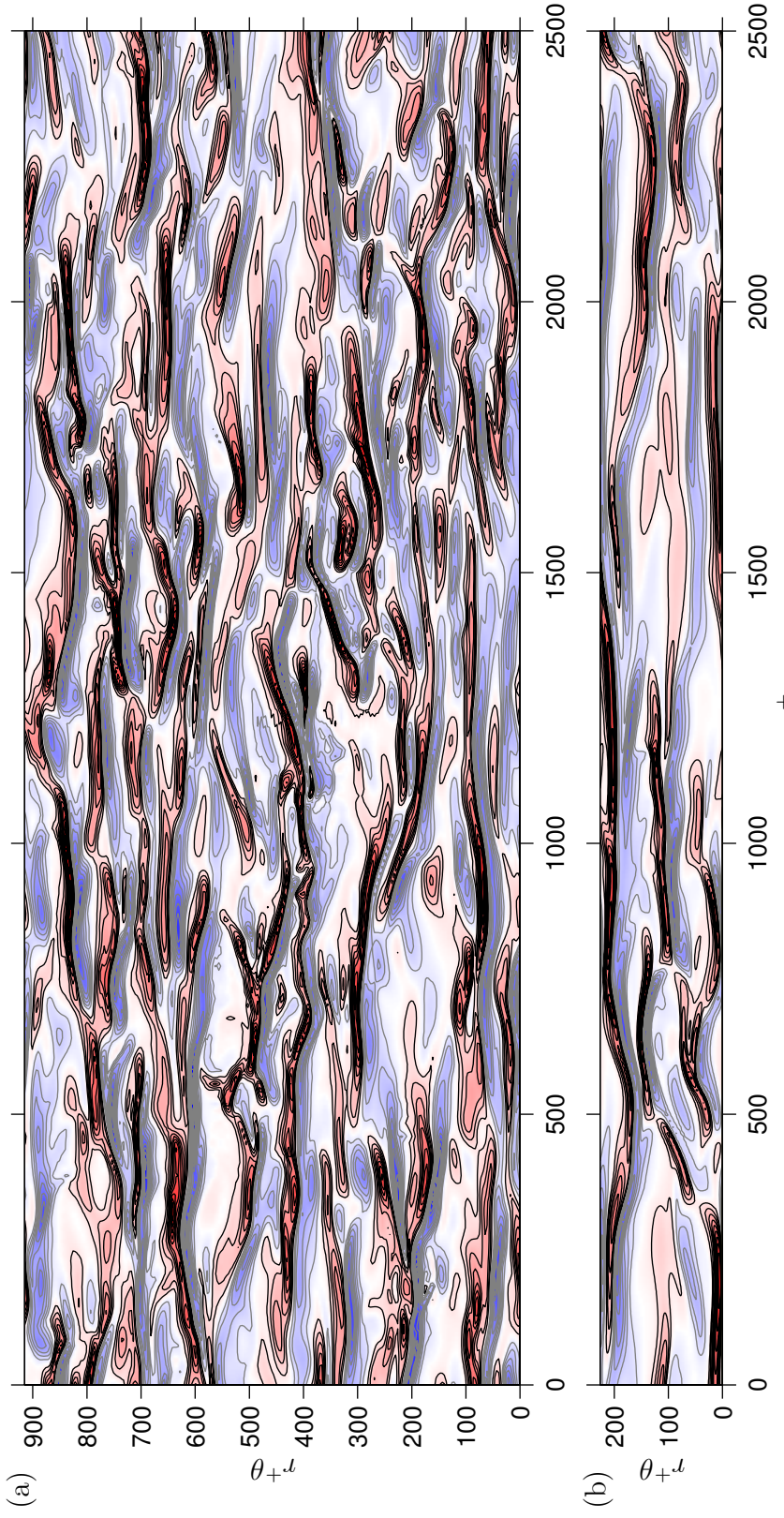

Figure 6.17: Instantaneous radial vorticity at $y^+ = 15$ for (a) $Re_a = 2600$, $b/a = 6$ and (b) $Re_a = 311$, $b/a = 41$. The contour increment is $0.06u_\tau^2/\nu$. Black contours and red shading indicate $\omega_r > 0$, grey contours and blue shading indicate $\omega_r < 0$.

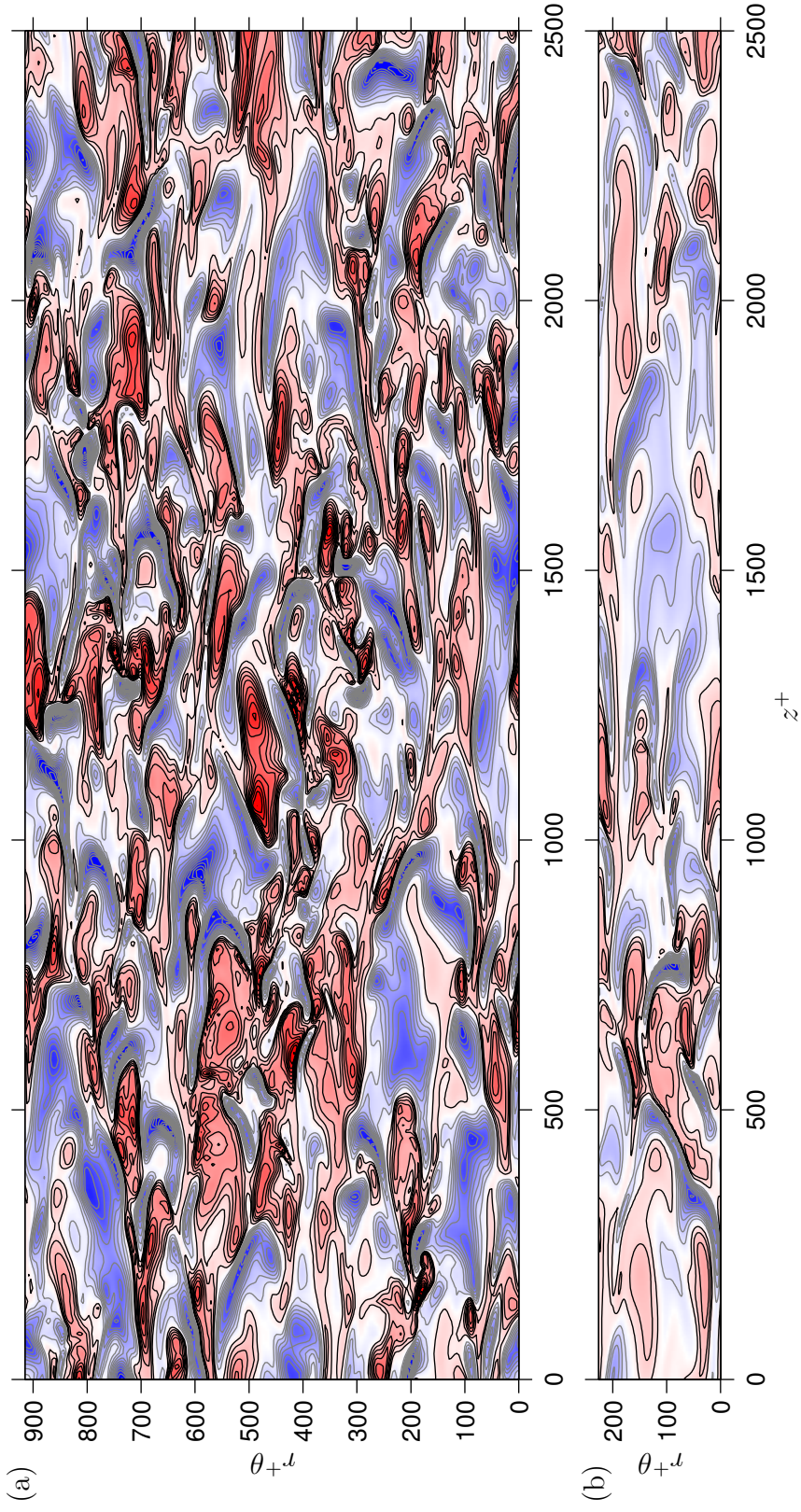

Figure 6.18: Instantaneous azimuthal vorticity fluctuations at $y^+ = 15$ for (a) $Re_a = 2600$, $b/a = 6$ and (b) $Re_a = 311$, $b/a = 41$. The contour increment is $0.06u_\tau^2/\nu$. Black contours and red shading indicate $\omega_\theta > 0$, grey contours and blue shading indicate $\omega_\theta < 0$.

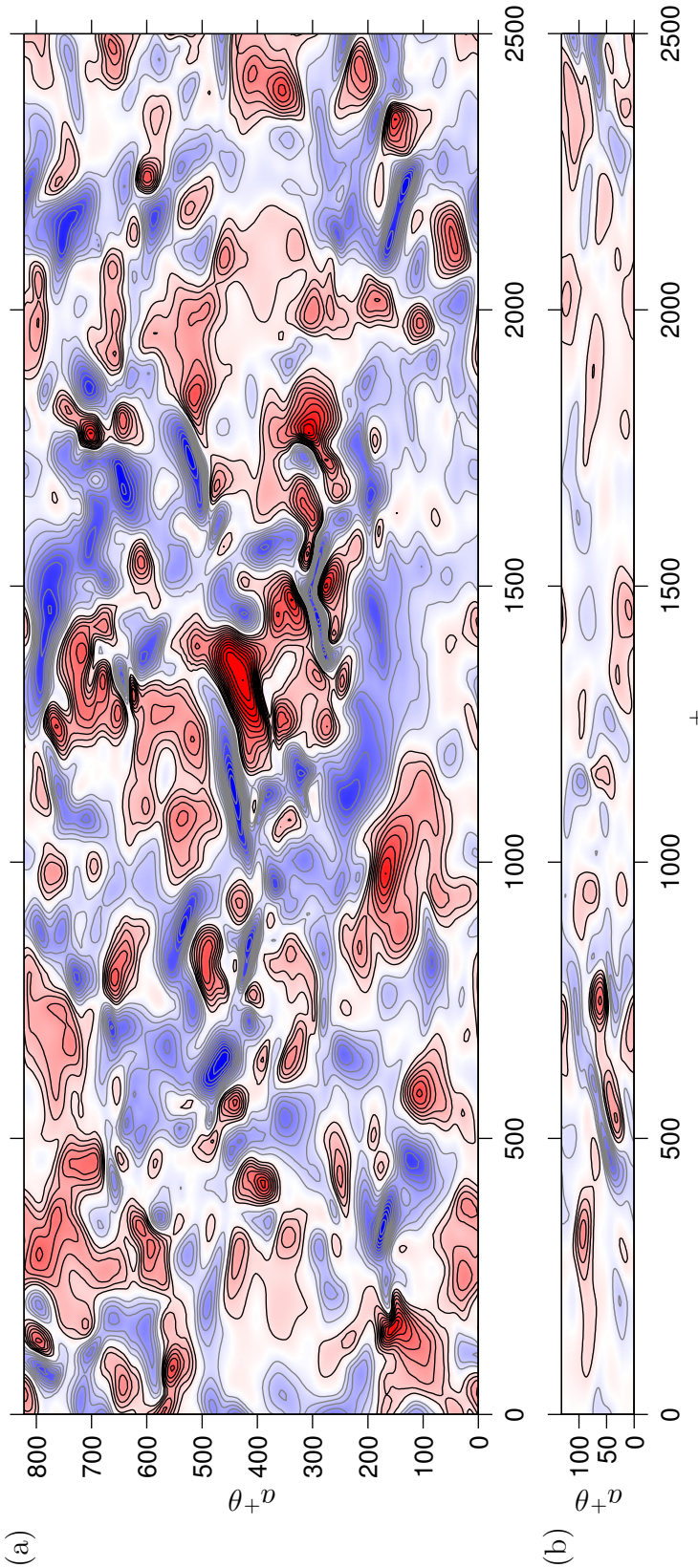

Figure 6.19: Instantaneous wall-pressure fluctuations for (a) $Re_a = 2600$, $b/a = 6$ and (b) $Re_a = 311$, $b/a = 41$. The contour increment is $0.5\tau_w$. Black contours and red shading indicate $p_w > 0$, grey contours and blue shading indicate $p_w < 0$.

6.2 Two-point Correlations

The typical dimensions (lengths and widths) of instantaneous flow structures may be estimated from two-point correlations of the flow variables as functions of streamwise or spanwise separation distance. The dimensions may be given numerical values, although the values depend on the criterion used to obtain them from the correlation functions. For the present work, it is instructive to examine the correlation functions directly, and where the numerical value of a correlation length is needed, it is based on the separation at which the correlation function decays to half of the peak value.

The two-point correlations as functions of azimuthal (spanwise) separation $r\Delta\theta$ and axial (streamwise) separation Δz are defined for the velocity fluctuations u by, respectively,

$$R_u[r\Delta\theta] = \overline{u[r\theta]\, u[r\theta + r\Delta\theta]} \,/\, \overline{u^2} \tag{6.1}$$

and

$$R_u[\Delta z] = \overline{u[z]\, u[z + \Delta z]} \,/\, \overline{u^2}. \tag{6.2}$$

The overbar indicates the average value calculated over the azimuthal and axial directions and over the temporal record. Normalisation of the correlation functions by the mean-square value of u ensures that the maximum value of R_u is unity when the separation distance is zero. Correlation functions for the pressure (R_p) are defined similarly.

Figure 6.20a shows the streamwise correlation functions of the axial (streamwise), azimuthal (spanwise) and radial (wall-normal) components of velocity at the wall-normal location $y^+ = 15$. The streamwise separation is expressed in wall units. Results are given for the present cylinder simulations (with some cases omitted for clarity) and the plane-channel calculations of Moser et al. [1999]. The correlation functions indicate that the typical streamwise lengths (in wall units) of the near-wall flow structures are of the same order in all of the flows considered. The correlation functions are little affected by the value of δ^+. The correlation lengths in the cylinder simulations appear to increase mildly as a^+ decreases. For example, as a^+ decreases from ∞ to 22, the correlation lengths corresponding to $R_u = 0.5$ for the axial, azimuthal and radial components increase, respectively, from $\Delta z^+ = 120, 50, 40$ to $\Delta z^+ = 150, 80, 80$.

The streamwise correlation functions in the outer flow, at the wall-normal location $y/h = 0.5$, are shown in figure 6.20b for the same flows as before. The streamwise separation is expressed as a proportion of h, which is the radial domain width or the plane-channel half-width. The correlation lengths in the plane-channel flows appear to approach a fixed proportion of h as δ^+ increases. For example, the

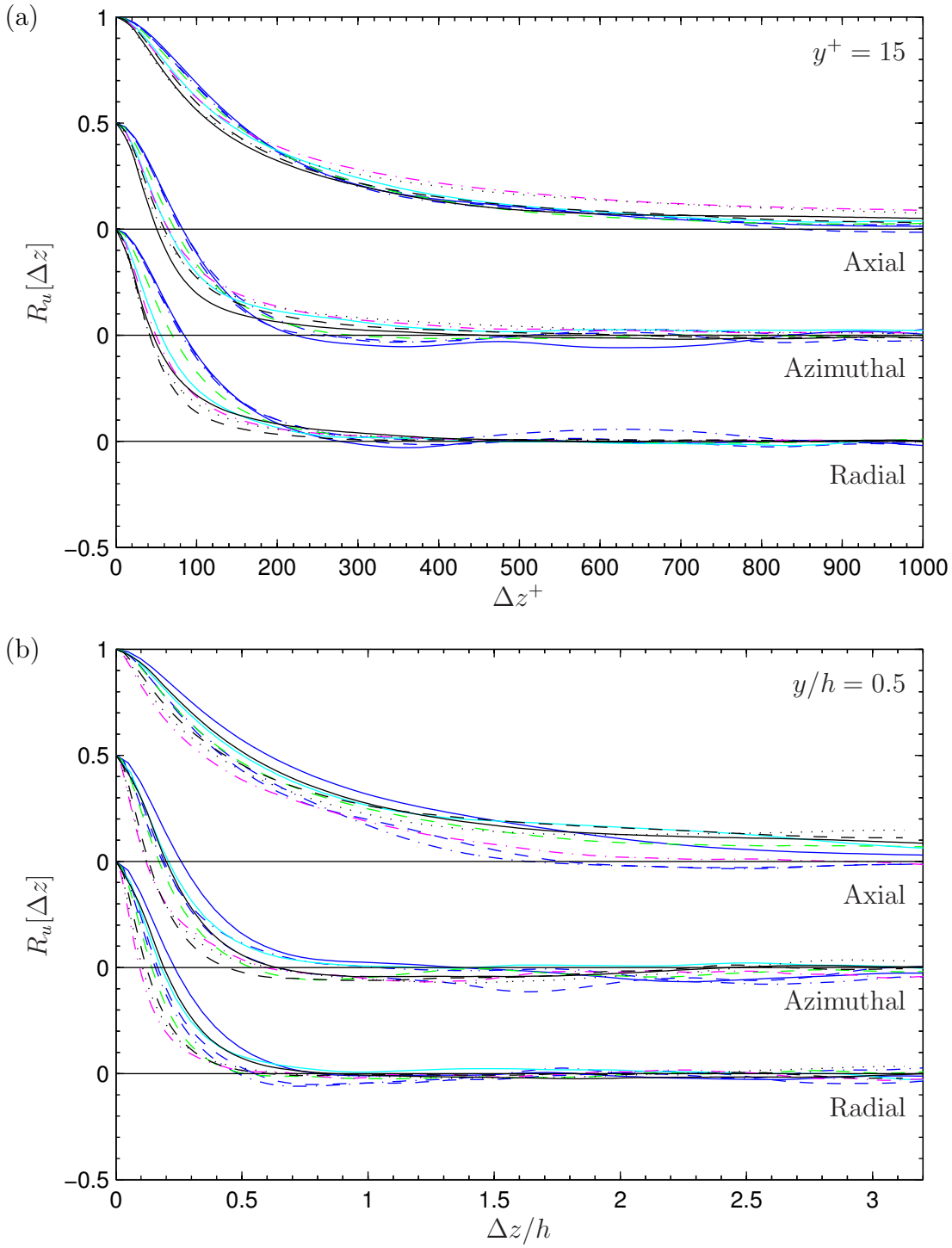

Figure 6.20: Streamwise (axial) two-point velocity correlations at (a) $y^+ = 15$ and (b) $y/h = 0.5$. Moser et al. [1999]: —— $\delta^+ \approx 149$; – – $\delta^+ \approx 326$; ····· $\delta^+ \approx 495$. Present data:

a^+	δ/a	δ^+	Line	a^+	δ/a	δ^+	Line	a^+	δ/a	δ^+	Line
21.9	7.82	171	——	21.5	14.0	302	– –	21.5	19.1	411	– · –
40.8	7.74	315	– –	146	1.18	173	——	163	4.92	802	– · –

correlation lengths corresponding to $R_u = 0.5$ for $\delta^+ = 149, 326, 495$ are, respectively, $\Delta z/h = 0.52, 0.43, 0.40$ for the axial component, $\Delta z/h = 0.20, 0.13, 0.12$ for the azimuthal component and $\Delta z/h = 0.19, 0.12, 0.11$ for the radial component. The correlation lengths for flow at a given δ^+ appear to increase slightly when the value of a^+ becomes small. For example, as a^+ decreases from ∞ to 22 with $\delta^+ \approx 170$, the correlation lengths (based on $R_u = 0.5$) for the axial, azimuthal and radial components increase, respectively, from $\Delta z/h = 0.52, 0.20, 0.19$ to $\Delta z/h = 0.60, 0.26, 0.23$.

It is observed that the "tail" of the correlation function for the axial velocity component (in figure 6.20b) decays to zero at different rates for different flows. At large separations, the correlation functions are influenced by computational issues such as the lengths of the simulation domain and the temporal record. Nevertheless, there is a consistent trend in the results for $a^+ \approx 22$, where the tail becomes shorter as δ/a increases. The shortening of the tail suggests that the occurrence of flow structures with sizes significantly larger than average is less and less likely as δ/a increases. It is not clear from the present data whether or not this effect is confined to flows with small a^+, because the simulations with larger a^+ are limited to $\delta/a < 8$.

Comparison of the streamwise correlation functions for the three components of velocity, at a given wall-normal location (figures 6.20a or b) in a given flow, reveals that the correlation length of the axial component is significantly greater than the correlation lengths of the other two components. Typical axial velocity structures in figure 6.3 do indeed appear to be longer than typical structures of radial and azimuthal velocity in figures 6.8 and 6.13. The reason for the difference between the streamwise correlation lengths of the velocity components is unclear at this stage.

Spanwise correlation functions of the velocity components at $y^+ = 15$ are shown in figure 6.21a. The correlation functions, with spanwise separation $r\Delta\theta$ expressed in wall units, are in reasonable agreement for all of the flows considered. For example, the spanwise separations at which $R_u = 0.5$ for the axial, azimuthal and radial components range, respectively, from $r^+\Delta\theta = 17, 20, 9$ to $r^+\Delta\theta = 21, 28, 12$. Most of the correlation functions exhibit a region of negative correlation, indicating that a given velocity structure is generally located adjacent to a structure of opposite polarity. The negative correlation becomes less pronounced as δ^+ increases in the plane-channel flows or as a^+ increases in the cylinder flows. An increase in δ^+ corresponds to an increase in the range of turbulence scales in the outer flow, and an increase in a^+ corresponds to an increase in the numbers of low- and high-speed streaks that are able to fit around the cylinder (as may be seen in figure 6.5, for example). The changes in the negative correlation due to increasing δ^+ and

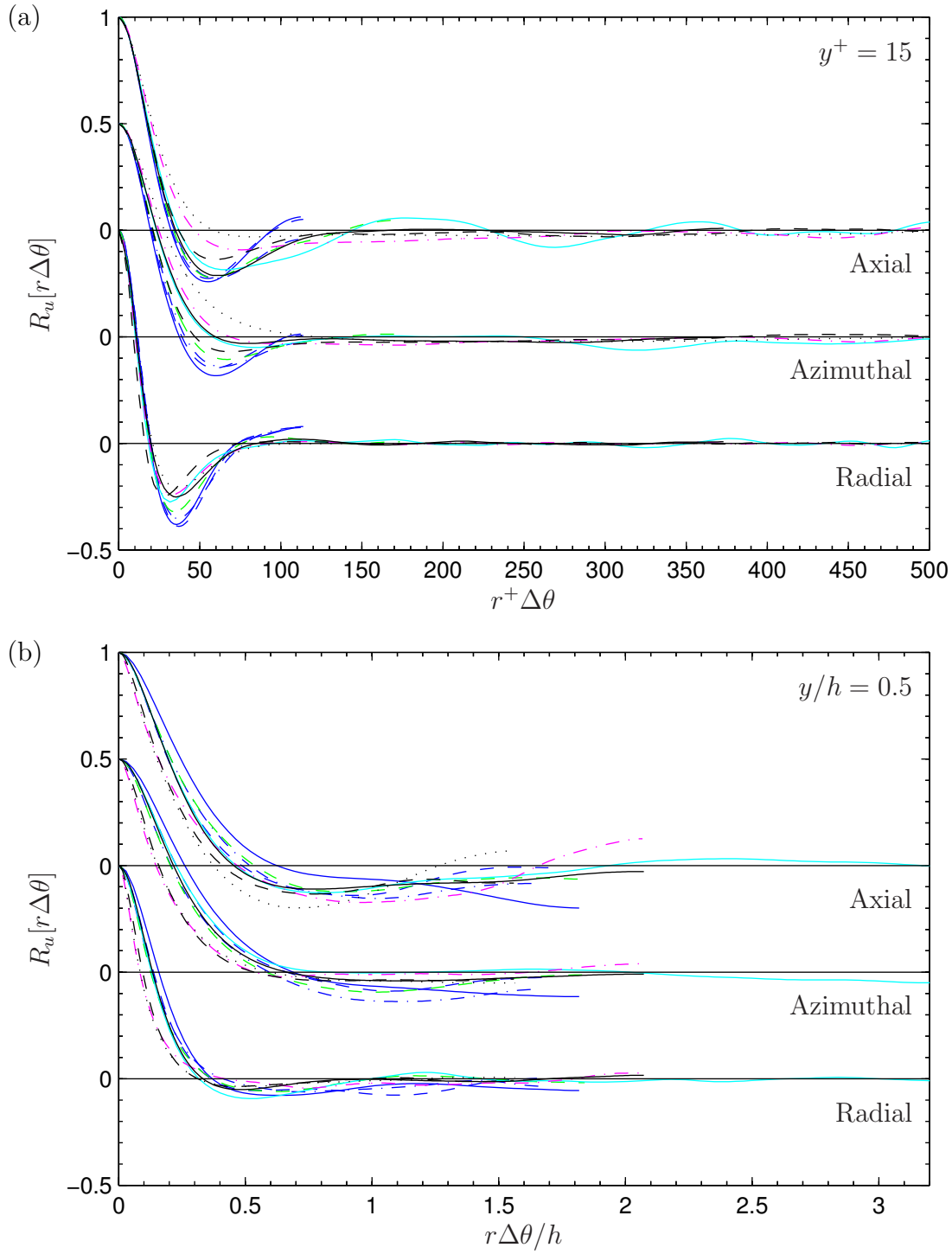

Figure 6.21: Spanwise (azimuthal) two-point velocity correlations at (a) $y^+ = 15$ and (b) $y/h = 0.5$. Moser et al. [1999]: —— $\delta^+ \approx 149$; – – $\delta^+ \approx 326$; ····· $\delta^+ \approx 495$. Present data:

a^+	δ/a	δ^+	Line	a^+	δ/a	δ^+	Line	a^+	δ/a	δ^+	Line
21.9	7.82	171	——	21.5	14.0	302	– –	21.5	19.1	411	·– ·–
40.8	7.74	315	– –	146	1.18	173	——	163	4.92	802	·– ·–

a^+ suggest that the relationship between neighbouring, near-wall flow structures becomes less consistent as the complexity of the flow increases.

Figure 6.21b shows spanwise correlation functions in the outer flow, at the wall-normal location $y/h = 0.5$. The correlation lengths, as a proportion of h, appear to be reasonably consistent for all of the flows considered. Subtle changes in the correlation lengths are observed when the values of δ^+ or a^+ become small. For example, as δ^+ decreases from 495 to 149 in the plane-channel flows, the spanwise correlation lengths (based on $R_u = 0.5$) for the axial, azimuthal and radial velocity components increase, respectively, from $r\Delta\theta/h = 0.15, 0.15, 0.09$ to $r\Delta\theta/h = 0.19, 0.22, 0.13$. As a^+ decreases from ∞ to 22 with $\delta^+ \approx 170$, the correlation lengths ($R_u = 0.5$) for the same velocity components increase from $r\Delta\theta/h = 0.19, 0.22, 0.13$ to $r\Delta\theta/h = 0.24, 0.26, 0.16$. These variations are similar in form to those of the streamwise correlations in figure 6.20b. Most of the correlation functions exhibit a region of slightly negative correlation, indicating that there is a relationship, albeit a weak one, between velocity structures of opposite polarity even well away from the wall.

Streamwise and spanwise correlations of wall-pressure fluctuations are shown in figure 6.22 for the same cylinder and plane-channel simulations as before. The streamwise and spanwise separations are expressed in wall units. The correlation functions are mildly dependent on a^+. As a^+ decreases from ∞ to 22 (with $\delta^+ \approx 170$), the streamwise correlation length (based on $R_p = 0.5$) increases from $\Delta z^+ = 35$ to $\Delta z^+ = 63$ while the spanwise correlation length decreases from $r^+\Delta\theta = 28$ to $r^+\Delta\theta = 15$. The increased streamwise correlation length for small a^+ may be due to the reduced complexity of the outer portion of the flow (as noted in relation to figures 6.1 and 6.2, for example), which may allow coherent pressure-sources to retain their identities over longer streamwise distances. The decreased spanwise correlation length of wall-pressure for flows with small a^+ is due, at least in part, to the decreased radius of wall curvature and the corresponding reduction in the spanwise length of the wall that faces pressure-sources of any given spanwise size.

When a^+ is large or infinite, as is the case in the plane-channel simulations, the influence of δ^+ on the wall-pressure correlation functions becomes noticeable. As δ^+ increases, both the streamwise and spanwise correlation lengths increase. For example, for the plane-channel flows with $\delta^+ = 149, 326, 495$, the respective streamwise correlation lengths ($R_p = 0.5$) are $\Delta z^+ = 35, 38, 41$ and the spanwise correlation lengths are $r^+\Delta\theta = 28, 32, 35$. The effect of δ^+ on the correlation lengths of wall-pressure is related to the correlation lengths of the pressure-sources associated with the velocity field. The correlation lengths of velocity are a quite consistent

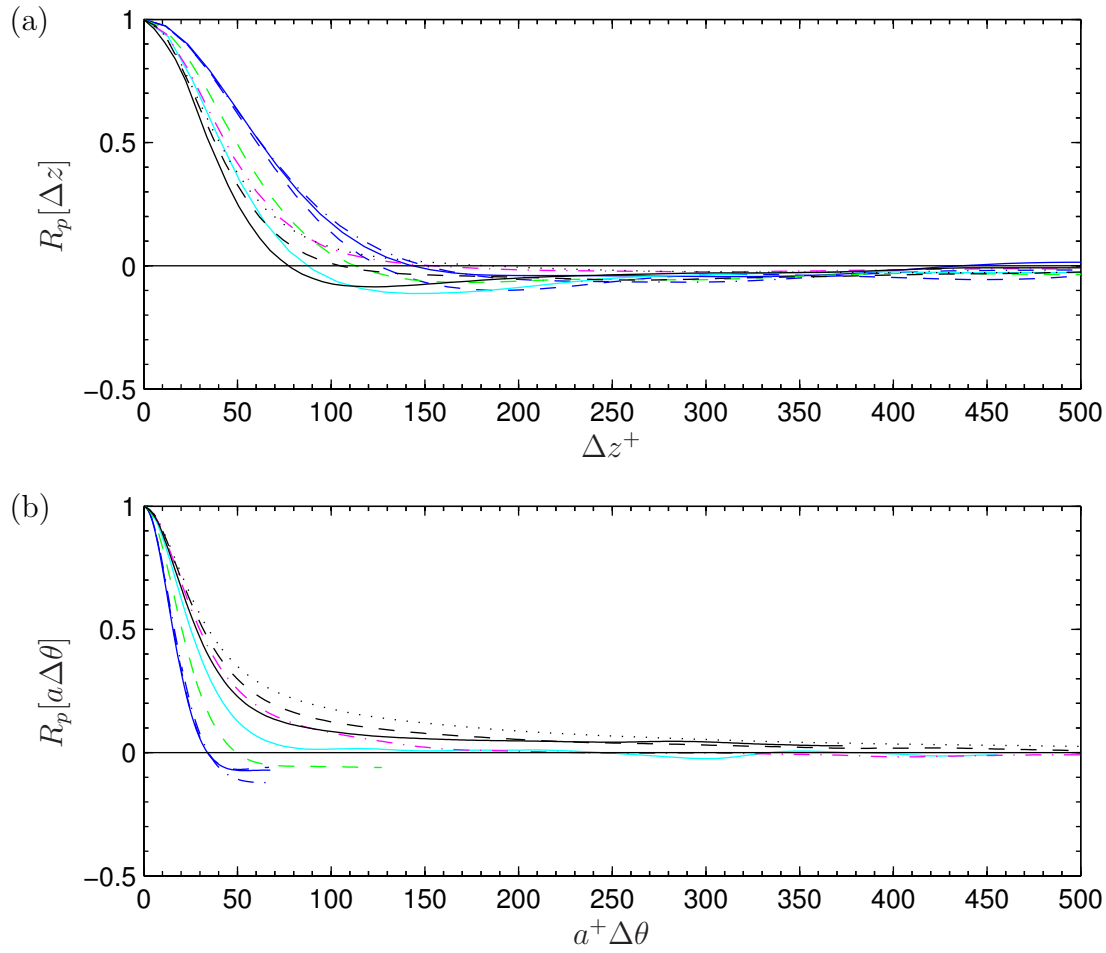

Figure 6.22: Two-point correlations of wall-pressure fluctuations as functions of (a) streamwise (axial) and (b) spanwise (azimuthal) separation. Moser et al. [1999]: —— $\delta^+ \approx 149$; – – $\delta^+ \approx 326$; ····· $\delta^+ \approx 495$. Present data:

a^+	δ/a	δ^+	Line	a^+	δ/a	δ^+	Line	a^+	δ/a	δ^+	Line
21.9	7.82	171	——	21.5	14.0	302	– –	21.5	19.1	411	·– –
40.8	7.74	315	– –	146	1.18	173	——	163	4.92	802	·– –

proportion of h at a given y/h location (figures 6.20b and 6.21b), suggesting that the correlation lengths of pressure-sources in the outer flow increase with h^+ (or δ^+).

6.3 Conditional Averages

The fundamental processes and events in a turbulent flow may be hidden when averaging is performed in space, time, wave-number or frequency. Conditional averaging allows particular types of flow structures or events to be investigated while avoiding the complications caused by random variations. In this section, the spatial structure of turbulent burst events is investigated by use of two different conditional averaging techniques applied to flow data generated by the present simulations.

The three-dimensional visualisation in figure 6.23 is for the ensemble average of slabs of flow data centred on individual burst events in flow case $Re_a = 3300$, $b/a = 7.3$. The location of burst events is detected based on local values of the Reynolds shear-stress $u_r u_z$ evaluated on an azimuthal-axial grid at $y^+ = 15$. Candidate locations are those for which the magnitude of $u_r u_z$ exceeds $3.5 u_r' u_z'$ with $u_r > 0$ and $u_z < 0$. The final list of burst event locations is prepared iteratively by finding the candidate location at which $u_r u_z$ is a maximum and eliminating neighbouring locations within a specified distance, repeating until no candidates remain. The resulting conditional average is visualised by means of isosurfaces for positive and negative values of velocity and vorticity components and the pressure field. Cones are used to indicate the resultant vector direction in the vicinity of the isosurfaces. The origin of the coordinate system in the azimuthal and axial directions corresponds to the detected location of the burst event.

By definition, the burst event (in figure 6.23) coincides with a low-speed streak of axial velocity where it lifts away from the wall. On either side, high-speed streaks of axial velocity are drawn inwards to replace the low-speed fluid. The vorticity field close to the wall is dominated by the azimuthal component, which lies beneath the low- and high-speed velocity streaks to satisfy the no-slip condition. The isosurfaces of radial vorticity correspond to the interfaces between low- and high-speed streaks of axial velocity. The axial vorticity is consistent with the wall-normal motion of the low-speed velocity streak and the spanwise, inward motion of the high-speed velocity streaks. The orientation of the cones suggests the presence of vortex loops around the burst structure. The pressure field indicates that the low-speed velocity streak is subject to a locally adverse pressure-gradient, while the high-speed velocity streaks are drawn inwards by a secondary pressure-gradient.

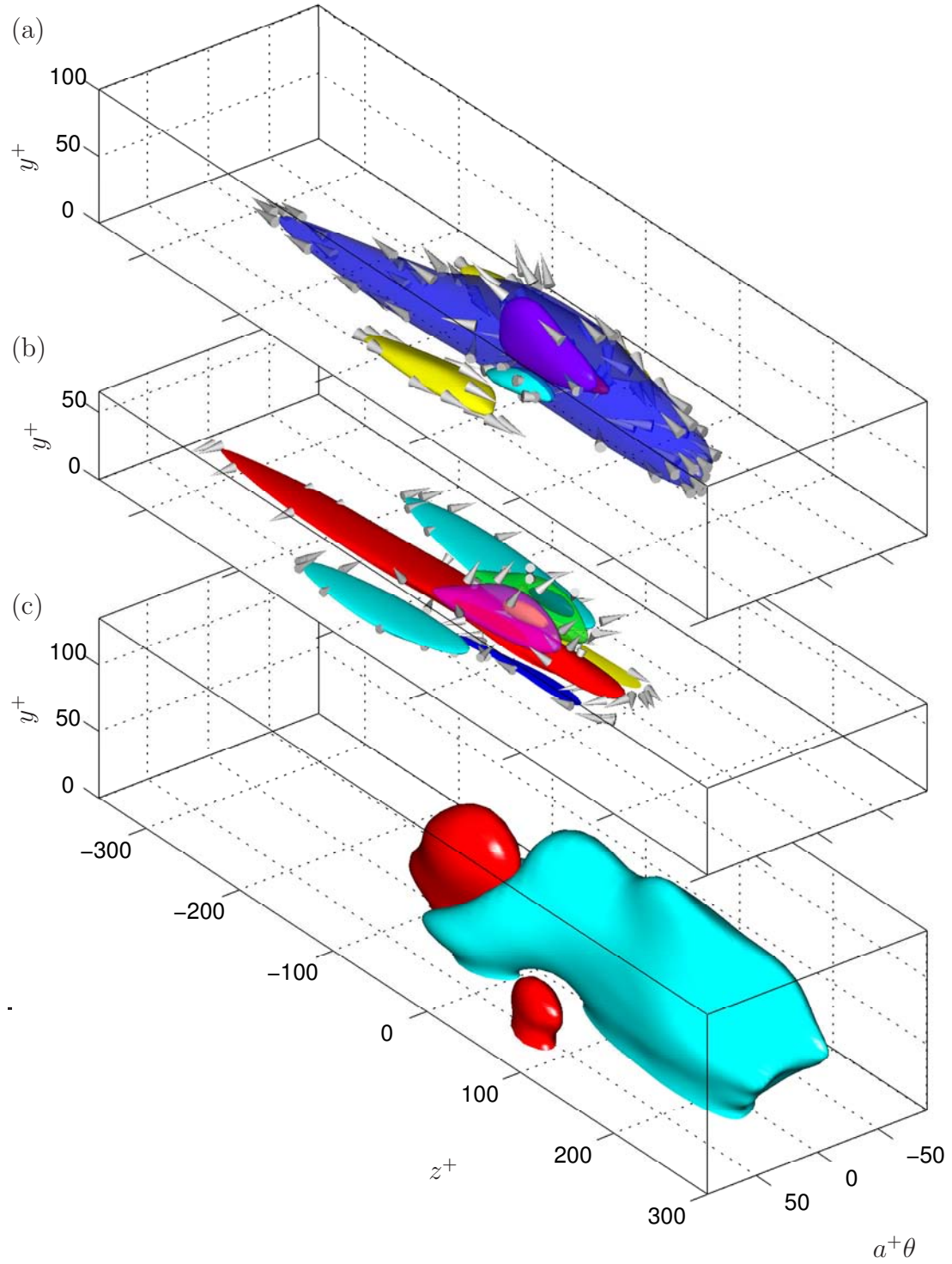

Figure 6.23: Average burst event conditioned on $u_r u_z < -3.5 u_r' u_z'$ with $u_r > 0$ and $u_z < 0$ at $y^+ = 15$ for flow case $Re_a = 3300$, $b/a = 7.3$. Visualisation of (a) velocity, (b) vorticity and (c) pressure. Cones indicate resultant vector direction. Isosurfaces for $\langle u_{r,\theta,z} \rangle = \pm \max[u_z']/3$, $\langle \omega_{r,\theta,z} \rangle = \pm \max[\omega_\theta']/3$, $\langle p \rangle = \pm \max[p']/3$. Components (+/−): axial (yellow/blue), radial (magenta/green), azimuthal and pressure (red/cyan). Transparency is used to reveal internal isosurfaces.

There are limitations inherent to the conditional averaging method used above. The averaged field is suitable for visualisation of spatial structure but does not allow causes to be distinguished from effects. Also, the azimuthal (spanwise) symmetry of the averaged spatial structure may not be entirely representative of a "typical" burst event. Guezennec, Piomelli, and Kim [1989] examine the streamwise circulation in spanwise slices through burst events detected in simulations of plane-channel flow. They find that the probability density function of the streamwise circulation is bimodal, so that structures with spanwise symmetry are less common than those with net streamwise circulation of one sign or the other. A similar analysis of the present cylinder data may be an interesting subject for future study.

In section 6.1, evidence is presented for the occurrence of large-scale turbulent cross-flows over the cylinder when a^+ is small and δ/a is large. One question that arises is whether or not the cross-flows are associated with changes in the mechanisms of turbulence generation. Bull and Dekkers [1993b] present conditional averages of signals from a radial array of hot-wire probes that demonstrate a link between cross-flow and so-called "low-speed spots", which are parcels of fluid associated with large negative spikes of u_z. In their experiment at $Re_a = 160$, the axial and radial components of velocity were ensemble-averaged for events with $u_z < -2u'_z$ at $y^+ = 6$. A similar process may be applied to the present simulation data. For each streamwise (r-z) plane of the mesh, candidate trigger locations are those where $u_z < -2u'_z$ at $y^+ = 13$. The list of candidate locations is weeded to avoid repeated triggers within the axial averaging interval. The slices of flow data centred on the final set of trigger locations are ensemble-averaged, as are the corresponding slices on the directly opposite side of the cylinder from each trigger location.

The results of the above procedure are shown in figure 6.24. The low-speed spot is clearly visible in the plane above the cylinder. However, unlike the experiment of Bull and Dekkers [1993b] for $Re_a = 160$, the present calculation for $Re_a = 311$ does not reveal any significant, related flow structures on the opposite side of the cylinder. A similar result is found for simulations at higher values of Re_a. The discrepancy may be due to the different values of a^+, which are $a^+ \approx 13$ for the experiment and $a^+ \gtrsim 22$ for the simulations. The number of velocity streaks around the cylinder circumference varies with a^+, as indicated by the near-wall slices of instantaneous axial velocity shown in figure 6.5. For $a^+ \approx 22$, there are typically four velocity streaks, and when $a^+ \approx 13$, roughly two streaks can be expected. When only two streaks are able to fit around the cylinder, it is reasonable to suppose that the motion of the streaks is interrelated, because the three-dimensional visualisation in figure 6.23 implicates at least a pair of axial velocity streaks, one low-speed and

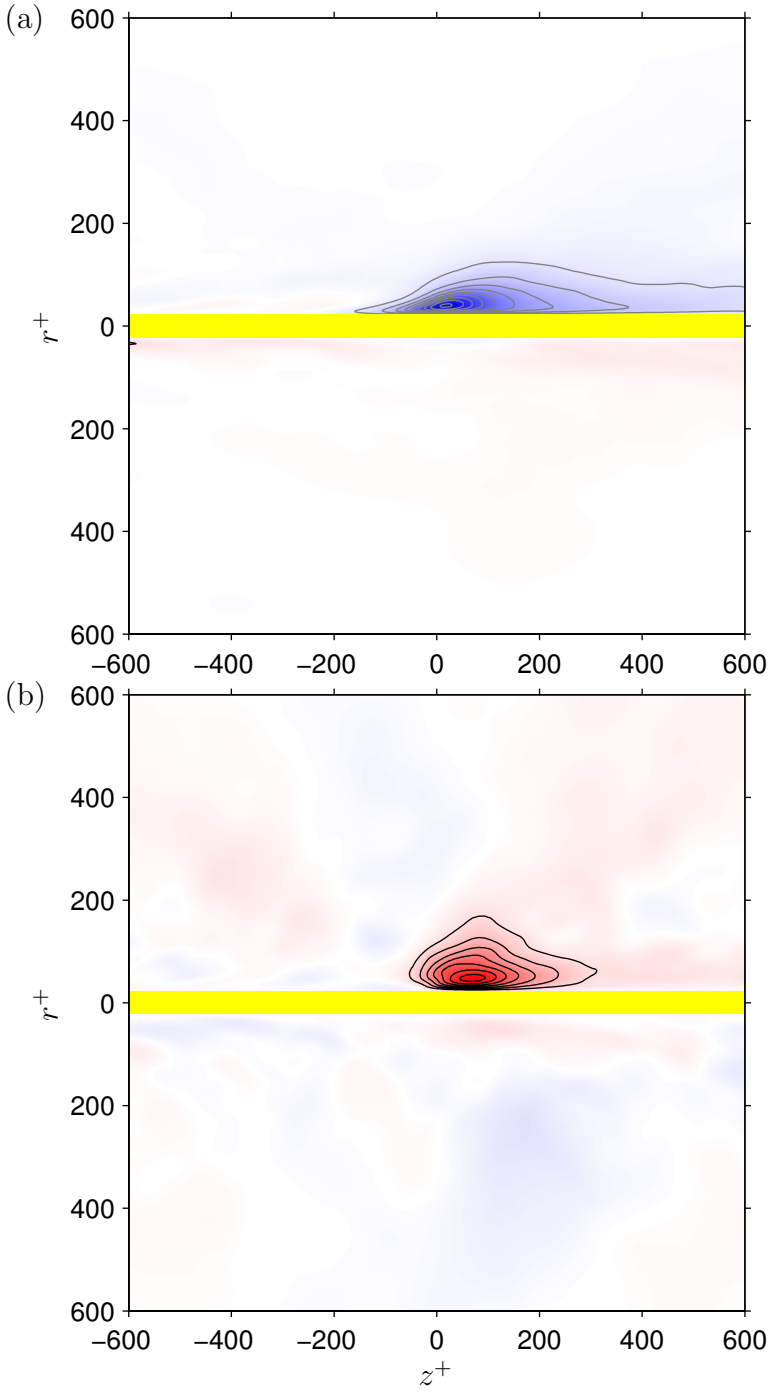

Figure 6.24: (a) Axial and (b) radial components of average velocity in r-z planes conditioned on $u_z < -2u'_z$ at $y^+ = 13$ (upper half-plane) for flow case $Re_a = 311$, $b/a = 31$. The contour increment is $0.1u_\tau$. Black contours and red shading indicate $u_{r,z} > 0$, grey contours and blue shading indicate $u_{r,z} < 0$.

one high-speed, in a typical burst event. Thus the link found by Bull and Dekkers [1993b] between cross-flow and low-speed spots may in fact be restricted to flow at extremely low values of a^+ and (hence) Re_a.

6.4 Summary and Conclusions

Instantaneous flow fields from the present simulations of turbulent boundary layers on cylinders in axial flow have been examined to reveal the structure of coherent regions of fluid that are present in the flow. Qualitative features of the flow structures have been investigated by visualisation of slice planes in two flows with similar δ^+ $(580, 527)$, δ/a much larger than unity $(27.6, 4.0)$ and either small or large a^+ $(21.0, 131)$. The streamwise and spanwise correlation functions of velocity and wall-pressure have been examined to reveal trends in the typical sizes of flow structures over a range of flows with different Reynolds numbers ($\delta^+ = 149$–802) and curvature parameters ($a^+ = 21.5$–∞, $\delta/a = 0$–19.1). The spatial structure of a particular type of turbulence event, the "burst", has been investigated by visualisation of conditionally averaged flow fields from two flows ($Re_a = 3300$, $b/a = 7.3$ and $Re_a = 311$, $b/a = 31$).

The visualisations of slice planes reveal bursts of low-speed fluid at various stages of ejection from the inner boundary layer, as well as regions of high-speed fluid sweeping towards the cylinder. Structures that lift away from the wall appear to lose their identity gradually as they interact with other structures or diffuse under the action of viscosity. Near the outer boundary of the computational domain, the radial motion of structures appears not to be inhibited by the presence of the boundary; this behaviour is an intentional characteristic of the simulation procedure.

Streamwise (r-z) slices of the azimuthal component of velocity (figures 6.13 and 6.14) reveal structures that are inclined to the wall at an angle of approximately 45°. The inclined structures correspond to vortical structures that become aligned as a result of vortex stretching, which acts to intensify the component of vorticity that is parallel to the axis of extension. Analyses of instantaneous vorticity fields from simulations of planar [Moin and Kim, 1985] and axisymmetric [Neves, 1992] boundary layers indicate that the vortex stretching is mainly driven by the mean shear-stress, whose principal axis is inclined at 45° to the solid wall.

The velocity structures in the transverse (r-θ) slice planes are small and finely spaced near the cylinder wall, while further out, the structures are typically larger. In flows with large δ/a, the largest flow structures can be considerably larger, in all directions, than the radius of the cylinder.

In the near-wall ($y^+ = 15$) slices of the axial component of velocity, the prevalent structures are streaks of low- and high-speed fluid that are long in the streamwise direction and narrow in the spanwise direction. The typical spanwise width of the streaks, in wall units, is similar for flows with large and small a^+, so that the number of streaks around the cylinder increases as the distance around the cylinder $\big(2\pi(a^+ + 15)\big)$ increases. Accordingly, the number of distinct structures in the transverse (r-θ) slices of the boundary layer, and the corresponding complexity of the flow, appears to increase with a^+. The difference in the number of structures is reflected in the skewness and flatness profiles of the velocity fluctuations, as discussed in section 4.5.

The streamwise and spanwise correlation functions of velocity for planar flows scale with wall units near the wall, at a given y^+ location, and with h (or δ) in the outer flow, at a given y/h (or y/δ) location. For the range of cylinder flows considered, the streamwise and spanwise correlation functions of velocity are found to scale in a similar fashion to those in the planar flows, although the correlation lengths appear to increase mildly, particularly in the outer flow, as a^+ is reduced to small values. The increased correlation lengths of velocity for small a^+ may be due to the reduced complexity of the flow (noted previously), which may allow coherent flow structures to retain their identities over longer streamwise and spanwise distances.

The wall-pressure correlation lengths, in wall units, increase slowly in both the streamwise and spanwise directions as δ^+ increases (for large values of a^+). The correlation lengths of wall-pressure are related to the correlation lengths of the pressure-sources associated with the velocity field. The correlation lengths of velocity, which are a quite consistent proportion of h at a given y/h location, suggest that the correlation lengths of pressure-sources in the outer flow increase with h^+ (or δ^+).

The correlation lengths of wall-pressure, with separations expressed in wall units, increase in the streamwise direction and decrease in the spanwise direction as a^+ decreases. The increased streamwise correlation lengths of wall-pressure for small a^+ may, once again, be due to reduced flow complexity, which may allow coherent pressure-sources to retain their identities over longer streamwise distances. The decreased spanwise correlation lengths of wall-pressure for small a^+ may be due to the decreased radius of wall curvature and the corresponding reduction in the spanwise length of the wall that faces pressure-sources of any given spanwise size.

The visualisations of slice planes through the flow with $a^+ = 21.0$ suggest that large-scale cross-flows over the cylinder occur at irregular intervals along the cylinder axis. The effects of cross-flow are much less obvious in the flow with $a^+ = 131$. It

is therefore tentatively concluded that cross-flows are most significant when a^+ is small and δ/a is large. In such a situation, there is typically a small number of structures distributed around the cylinder at a given streamwise location, and many of the structures are significantly larger than the cylinder cross-section. At irregular intervals along the cylinder, the structures can be expected to interact in such a way that there is coherent motion of fluid across the cylinder. The large size of the structures relative to the cylinder ensures that the cross-flow motion is not inhibited by the cylinder wall.

One question that arises concerning the large-scale cross-flows is whether or not they are associated with changes in the mechanisms of turbulence generation. Bull and Dekkers [1993b] present conditional averages of signals from a radial array of hot-wire probes that demonstrate a link between cross-flow and low-speed spots. In their experiment at $Re_a = 160$ ($a^+ \approx 13$), the axial and radial components of velocity were ensemble-averaged for events with $u_z < -2u'_z$ at $y^+ = 6$. A similar process has been applied to the present simulation data. However, unlike the measurements of Bull and Dekkers, the present calculations for $Re_a \geq 311$ ($a^+ \gtrsim 22$) do not reveal any significant, related flow structures on opposite sides of the cylinder. Thus the link found by Bull and Dekkers [1993b] between cross-flow and low-speed spots appears to be limited to flow at extremely low values of Re_a and a^+.